Clemson University
TigerPrints

All Theses | Theses

12-2011

A New Approach to Dynamic Modeling of Continuum Robots

Nivedhitha Giri
Clemson University, ngiri@g.clemson.edu

Follow this and additional works at: https://tigerprints.clemson.edu/all_theses

Part of the Robotics Commons

Recommended Citation
Giri, Nivedhitha, "A New Approach to Dynamic Modeling of Continuum Robots" (2011). *All Theses*. 1227.
https://tigerprints.clemson.edu/all_theses/1227

This Thesis is brought to you for free and open access by the Theses at TigerPrints. It has been accepted for inclusion in All Theses by an authorized administrator of TigerPrints. For more information, please contact kokeefe@clemson.edu.

A NEW APPROACH FOR DYNAMIC MODELING OF CONTINUUM ROBOTS

A Thesis
Presented to
the Graduate School of
Clemson University

In Partial Fulfillment
of the Requirements for the Degree
Master of Science
Electrical Engineering

---

by
Nivedhitha Giri
December 2011

Accepted by:
Dr. Ian D. Walker, Committee Chair
Dr. Keith E. Green
Dr. Timothy C. Burg

ABSTRACT

In this thesis, a new approach for developing practically realizable dynamic models for continuum robots is proposed. Based on the new dynamic models developed, a novel technique for analyzing the capabilities of continuum manipulators to be employed in various real world applications has also been proposed and developed.

A section of a continuum arm is modeled using lumped model elements (masses, springs and dampers). It is shown that this model, although an approximation to a continuum structure, can be used to conveniently analyze the dynamics of the arm with suitable tradeoff in accuracy of modeling. This relatively simple model is more plausible to implement in an actual real-time controller when compared to other techniques of modeling continuum arms. Principles of Lagrangian dynamics are used to derive the expressions for the generalized forces in the system. The force exerted by McKibben actuators at different pressure level – length pairs is characterized and is incorporated into this dynamic model. The constraints introduced in the analytical model conform to the physical and operational limitations of the Octarm VI continuum robot manipulator. The model is validated by comparing the results of numerical simulation with the physical measurements of a continuum arm prototype built using McKibben actuators.

Based on the new lumped parameter dynamic model developed for continuum robots, a technique for deducing measures of manipulability, forces and impacts that can be sustained or imparted by the tip of a continuum robot has been developed. These measures are represented in

the form of ellipsoids whose volume and orientation give information about the various functional capabilities (end effector velocities, forces, and impacts) of the arm at a particular configuration. The above mentioned ellipsoids are exemplified for different configurations of the continuum section arm and their physical significance is analyzed. The new techniques proposed and methodologies adopted in this thesis supported by experimental results represent a significant contribution to the field of continuum robots.

DEDICATION

To my dad, Mr. S. Giri, whom I look upon as an embodiment of diligence and self-motivation

To my mom, Mrs. Chithra Giri who inculcated the qualities of composure and perseverance in me

To my sister, Nandhini Giri who has been a cheerful companion and a guide

ACKNOWLEDGEMENTS

I offer my deepest gratitude to my research advisor, Dr. Ian D. Walker who was abundantly helpful and offered invaluable inputs and assistance in guiding me throughout my research and thesis writing. I attribute the technical achievement of my Master's degree to his encouragement and effort without which this thesis would not have been completed. I would also like to thank Dr. Keith Green and Dr. Timothy Burg for serving on my committee and providing suggestions for improving my thesis.

I must also thank my friends and peer Graduate students, particularly Balajee Ananthasayanam, Prabhu Shankar, Varun Prabhu and Harshwardhan Karve whose insightful views resulting from our casual discussions about research had a major impact in shaping my approaches to problem solving.

Finally, I thank my parents and sister, who provided me with immense moral support on various issues throughout my Graduate student life.

TABLE OF CONTENTS

TITLE PAGE ..... **i**
ABSTRACT ..... **ii**
DEDICATION ..... **iv**
ACKNOWLEDGEMENTS ..... **v**
TABLE OF CONTENTS ..... **vi**
LIST OF TABLES ..... **viii**
LIST OF FIGURES ..... **x**
1. INTRODUCTION **1**
2. CONTINUUM ROBOTS IN GRASPING **7**
2.1 BACKGROUND 7
2.2 CONTINUUM GRASPING - CONCEPT 9
2.3 CONTINUUM GRASPING - PRACTICE 11
2.4 DISCUSSION 22
3. EXTENSOR MUSCLE CHARACTERIZATION **27**
3.1 LITERATURE REVIEW 27
3.2 CONTRACTORS AND EXTENSORS 33
3.3 EXTENSOR CHARACTERIZATION 34
4. EFFICIENT LUMPED PARAMETER DYNAMIC MODEL OF A CONTINUUM ARM SECTION **43**
4.1 THE PROBLEM AND MOTIVATION 43
4.2 MODELING PRINCIPLES 45
4.3 DERIVATION OF THE THREE-MODULE MODEL 46
4.4 MODEL VALIDATION 54
4.4.1 NUMERICAL RESULTS 56
4.5 ALTERNATIVE DYNAMIC MODEL 61
5. ELLIPSOID MEASURES FOR A CONTINUUM ARM SECTION **68**
5.1 BACKGROUND 68
5.2 ELLIPSOID MEASURES 70

5.3 NEW ELLIPSOIDS: ANALYSIS AND RESULTS 73
6. CONCLUSIONS AND FUTURE WORK 93
6.1 CONCLUSIONS 93
6.2 SUGGESTIONS FOR FUTURE WORK 95
APPENDIX 97
Appendix A: Actuator Parameters 97
Appendix B: Dynamic Modeling 99
REFERENCES 104

LIST OF FIGURES

2.1 Picture of Octarm VI with its three sections and actuators marked....12
2.2 Difference in actuator pressures resulting in bending
of a section (originally appeared in [31]....12
2.3 Kinematics of a single section of a continuum arm....14
2.4 Octarm grasping a spherical object – continuum grasp....15
2.5 Using two sections and one section for grasping the same object....16
2.6 Octarm grasping a compliant object....17
2.7 Object held by contact points....18
2.8 Mix of continuum and point contacts....19
2.9 Grasping fragile objects – using parallel jaw gripper(unsafe grasp);Octarm....20
2.10 Octarm – Grasping and acquiring a moving object....21
3.1 McKibben actuator....28
3.2 Components of air muscles....28
3.3 Actuator model....30
3.4 Actuator characterization....35
3.5 Actuator forces at zero extension....36
3.6 Actuator forces at different % of extension....37
3.7 Interpolation of experimental actuator force data....39
3.8 Stiffness characterization....41
4.1 Octarm VI, individual actuators and planar equivalent prototype....46
4.2 Parameters in spatial and planar configurations (originally appeared in [54])....46
4.3 Assumed structure for analytical model of a section of a continuum arm....48
4.4 Experimental setup for taking measurements from the prototype……..56
4.5 Single module of the model....62
4.6 Reduced model....63
4.7 Extension and bending....64
5.1 Manipulability ellipsoids....75
5.2 manipulating force ellipsoids....76

5.3 Dynamic impact ellipsoids.....77
5.4 Generalized impact ellipsoids.....77
5.5 Ellipsoids drawn for equal pressures in both actuators.....79
5.6 Unequal pressures in both actuators (less curvature of bending) 82
5.7 Unequal pressures in both actuators (more curvature of bending) 85
5.8 Impact ellipsoids for uniform variation of mass.....87
5.9 Impact ellipsoids when terminal mass is increased 89

LIST OF TABLES

2.1 Compliance of all three sections (measured in a direction perpendicular to the length of the arm) 22
2.2 Approximate curvature of sections 23
2.3 Payload of the Octarm. 24
2.4 Actuator parameters 24
3.1 Actuator forces at zero extension 36
4.1 Prototype dimensions 55
4.2 Measurements and numerical results with gravity in the system (actuator force as a variable of length) 57
4.3 Measurements and numerical results without gravity in the system (actuator force as a variable of length) 57
4.4 Measurements and numerical results with gravity in the system (constant actuator force) 58
4.5 Measurements and numerical results without gravity in the system (constant actuator force) 59

CHAPTER ONE

INTRODUCTION

1.1 OVERVIEW

In this thesis, new ideas and models for modeling continuum robots are presented. The results focus on several of the existing open issues in dynamic modeling of continuum robots. A novel step by step approach for modeling a single section of a continuum arm is presented in this document. A continuum arm prototype was also built to validate this model. Ellipsoid measures for analyzing practical capabilities at the tip of a continuum section are developed and analyzed. The overall work presented in this thesis makes a theoretical contribution to the field of continuum robotics aimed at making these robots a more practical option in various real world applications.

Continuum robots represent a class of robots that have a biologically inspired form characterized by flexible backbones and high degrees-of-freedom structures [1]. The idea of creating "trunk and tentacle" robots, (in recent years termed continuum robots [1]), is not new [2]. Inspired by the bodies of animals such as snakes [3], the arms of octopi [4], and the trunks of elephants [5], [6], [7], researchers have been building prototypes for many years. A key motivation in this research has been to reproduce in robots some of the special qualities of the biological counterparts. This includes the ability to "slither" into tight and congested spaces, and (of particular interest in this work) the ability to grasp and manipulate a wide range of objects, via the use of "whole arm manipulation" [8], i.e. wrapping their bodies around objects,

conforming to their shape profiles. Hence, these robots have potential applications in whole arm grasping and manipulation in unstructured environments such as rescue operations.

Most of these robots built so far fall in the range of medium-scale (roughly 1 meter length) manipulators. However, some initial work in combining multiple continuum bodies into "multi-fingered" versions has been demonstrated [9], [10],[11].

Theoretically, the compliant nature of a continuum robot provides infinite degrees of freedom to these devices. However, there is a limitation set by the practical inability to incorporate infinite actuators in the device. Most of these robots are consequently underactuated (in terms of numbers of independent actuators) with respect to their anticipated tasks. In other words they must achieve a wide range of configurations with relatively few control inputs. This is partly due to the desire to keep the body structures (which, unlike in conventional rigid-link manipulators or fingers, are required to directly contact the environment) "clean and soft", but also to exploit the extra control authority available due to the continuum contact conditions with a minimum number of actuators [12]. For example, the Octarm VI continuum manipulator, discussed frequently in this Thesis, has nine independent actuated degrees-of-freedom with only three sections.

Continuum manipulators differ fundamentally from rigid-link and hyper-redundant robots [13] by having an unconventional structure that lacks links and joints. Hence, standard techniques like the Denavit-Hartenberg (D-H) algorithm [21] cannot be directly applied for developing continuum arm kinematics. Moreover, the design of each continuum arm varies with

respect to the flexible backbone present in the system, the positioning, type and number of actuators. The constraints imposed by these factors make the set of reachable configurations and nature of movements unique to every continuum robot. This makes it difficult to formulate generalized kinematic or dynamic models for continuum robot hardware. Chirikjian and Burdick were the first to introduce a method for modeling the kinematics of a continuum structure by representing the curve-shaping function using modal functions [14]. Mochiyama used the Serret-Frenet formulae to develop kinematics of hyper-degrees of freedom continuum manipulators [15]. For details on the previously developed and more manipulator-specific kinematics of the Rice/Clemson "Elephant trunk" manipulator, see [16], [17], [6]. For the Air Octor and Octarm continuum robots, more general forward and inverse kinematics have been developed by incorporating the transformations of each section of the manipulator (using D-H parameters of an equivalent virtual rigid link robot) and expressing those in terms of the continuum manipulator section parameters [18]. The net result of the work in [6], [14]-[18] is the establishment of a general set of kinematic algorithms for continuum robots. Thus, the kinematics (i.e. geometry-based modeling) of a quite general set of prototypes of continuum manipulators has been developed and basic control strategies now exist based on these.

The development of analytical models to analyze continuum arm dynamics (i.e. physics-based models involving forces in addition to geometry) is an active, ongoing research topic in this field. A detailed discussion of research done in this area in the recent past is given in Chapter 4. From a practical perspective, the modeling approaches currently available in the literature prove to be very complicated and a dynamic model which could be conveniently implemented in an actual device's real-time controller has not been developed yet. The absence of a

computationally tractable dynamic model for these robots also prevents the study of interaction of external forces and the impact of collisions on these continuum structures. This impedes the study and ultimate usage of continuum robots in various practical applications like grasping and manipulation, where impulsive dynamics [19], [20] are important factors. Although continuum robotics is an interesting subclass of robotics with promising applications for the future, from the current state of the literature, this field is still in its stages of inception. This thesis focuses on providing solutions for several of the current open issues by presenting a new, more tractable approach for dynamic modeling and a generalized technique (which follows subsequently from the dynamic model) for analyzing the characteristics of continuum robots in different configurations. This represents a novel contribution made by this thesis to the future of continuum robots in real world applications.

The contents of this thesis are organized into six chapters. The second chapter (continuum robots in grasping) provides the reader with a detailed discussion and analysis of one of the main potential applications for continuum robots - continuum arm manipulation/grasping. Results of experiments on continuum grasping using the Octarm VI continuum manipulator are presented in Chapter 2, highlighting various points that emphasize the need for a computationally tractable dynamic model to aid in better operation of the arm for the grasping application. This chapter also reviews the kinematics and operation of the Octarm VI continuum robot hardware (used to "ground" the theoretical development later in this thesis) and presents and catalogs various parameters of the arm that were measured and calculated in order to quantify the nature of grasping performed by this device. The work presented in this chapter is published in [54] and [65].

The third chapter covers characterization of McKibben actuators, a.k.a artificial air muscles, which form the backbone of many continuum robots (including Octarm IV) structure. The first half of this chapter explains the principle of operation of these artificial air muscles and the existing literature on their modeling. It is seen that models for extensor actuators, the type used for continuum robots, are lacking. The second part of this chapter introduces a new approach to modeling the forces and stiffness of these extensor muscles, and represents one of the novel contributions of this Thesis.

The fourth chapter introduces a new approach to the derivation of an analytical model for a section of a continuum arm. The approach is based on the combination of simple lumped parameter elements, and is shown to be computationally tractable while also sufficiently well-matched to continuum robot hardware. The actuator modeling introduced in the previous chapter is included within this model. Results of numerical simulations are compared with measurements taken from a planar continuum arm prototype. Alternative ideas on modeling continuum arm sections following the same approach (lumped parameter elements) are also suggested in this chapter. The main results of this chapter are to be published in [66].

The fifth chapter presents a new technique for quantifying measures of velocity and force manipulability, and the ability to sustain impacts at the tip of continuum robots. This technique is based on the new dynamic model for continuum robots introduced in Chapter 4. The implications of using this technique for different manipulator configurations are presented and interpreted.

Chapter 6 summarizes the major topics covered in this thesis and their significance. The discussion in this chapter also provides suggestions for potential improvements to this work and directions for future research.

CHAPTER TWO

CONTINUUM ROBOTS IN GRASPING

One of the major applications of continuum robots that have been proposed is the use of these robots in grasping. This chapter starts with a brief introduction on robot grasping and then explains the concept of continuum robot grasping and validation of the concept by experiments using the Octarm VI continuum robot. The chapter ends with a note on measures for quantifying continuum robot grasping and the need for a dynamic model that will enable us to study the effects of impact and other forces incurred in practical continuum arm grasping. The results of the experiments conducted on the Octarm VI and presented in this chapter were originally published in [54], [65].

1.1 BACKGROUND

Grasping has been a core topic in robotics since the inception of the field. The classic "pick and place" strategy for robot manipulators is core to many industrial applications. Typically, in this situation grasping is achieved using a parallel jaw gripper at the end of the manipulator. This is a simple and reliable strategy, but limits the set of graspable objects to those that fit into the shape and scale of the gripper.

Researchers have long sought to improve the versatility and dexterity of robot end effectors. Typically the strategy has been influenced by the readily available case study of the human hand. Many multi-fingered hand designs have been proposed, constructed, and analyzed

through the years. For an extensive survey conducted over 30 years ago, see [22]. For a more recent survey of the field, see [23]. Most robot hands feature the anthropomorphic design of a thumb and opposable fingers. However, other designs have been proposed. For example, the three-fingered Barrett Hand [24] features the (quite non-anthropomorphic) design of rotating one finger around its "palm", so it can serve at times as an opposable thumb, and at other times as a conventional finger.

However, despite steady improvement in the performance of multi-fingered robot hands, the industrial standard today remains the parallel jaw gripper. This is in part due to the inherent complexity of the human hand that multi-fingered robot hands seek to emulate. It is difficult to produce a dexterous yet reliable hand at the scale desired for most applications. This difficulty is amplified by the need to mount the hands at the end of robot manipulators, which in turn imposes significant restrictions on hand weight and packaging.

Instead of using the human hand for motivation, in this thesis adopt concepts from biological "tongues, trunks, and tentacles" are adopted. This results in robot grasping based on "invertebrate" continuum robots as opposed to "vertebrate" fingers in conventional robot hands. This can lead to simpler, lower degree-of-freedom designs. Rather than analyzing special classes of grasping, we seek to widen the range of graspable objects via the judicious inclusion of inherent compliance in the hardware. One notable feature of continuum structures is that, while kinematically redundant versions have been developed [6], [13], many prototypes have been designed to be under-actuated (in terms of numbers of independent actuators) with respect to their anticipated tasks. This is partly due to the desire to keep the body structures (which, unlike

in conventional rigid-link manipulators or fingers, are required to directly contact the environment) “clean and soft”, but also to exploit the extra control authority available due to the continuum contact conditions with a minimum number of actuators [12]. Continuum manipulators can be approximated by the operation of a multi-linked, under-actuated chain, but the kinematics, actuation and control strategies employed are very different from the former.

2. 2 CONTINUUM GRASPING- CONCEPT

The ability to exploit continuum contact – particularly line contact – to restrain and manipulate objects is well-established. Consider for example the example of spinning tops by pulling on strings initially wrapped around their bodies [25], or the dynamic manipulation of objects using whips [26]. The physics of these activities, and related activities such as flycasting [27], are well established. The situation of manipulation of objects using ropes has also been the subject of interest in the robotics community [28].

The above real-world examples demonstrate situations in which low (often single) degree of freedom inputs, when well planned and executed, are sufficient to control higher-dimensional behavior of the manipulated environment. It is clear that the ability to “wrap around” an object presents a significant mechanical advantage, which if exploited carefully, can afford a complex behavior from a simple, low degree of freedom actuation strategy. A key issue for developers of continuum robots is to what extent this concept can be used in practice to perform useful grasping with under-actuated systems.

In grasping, as discussed above, the key attribute of continuum robots is their capability, via their inherent ability to bend at any point along their structure, to adapt their shape to conform to the perimeter of objects to be grasped. In theory, this ability could be exploited, if the continuum robot were sufficiently long and powerful, to "wrap around an object in all directions and completely constrain it". This suggests an alternative to the traditional way of thinking about grasp analysis as the net effect of a finite number of (local) contact locations. Conceptually, continuum (line) contact can be viewed as placing an infinite number of fingers in a tunable line around the surface of an object to be grasped. The inference is that the object can be "surrounded" by contacts over a sufficiently wide range of its surface to achieve, for example, full force- or form-closure [23], and thus stable grasping.

The engineered situation however can never be quite as described above. While continuum contact can be maintained around the complete perimeter of an object, it is not feasible to apply arbitrary forces at given points on the perimeter, as if there were "infinite fingers". To do this would require in general an infinite number of actuators, corresponding to the infinite number of degrees of freedom theoretically available in the robot structure. In practice, although there are numerous different design strategies [12], continuum robots possess a small finite number of actuators, with the remaining (infinite) degrees of backbone freedom determined at each instant implicitly, via a combination of backbone materials properties, actuation forces, and external loading [12]. Despite this, continuum robot grasps do indeed tend to be quite robust to external disturbances [12], [29]. The passive compliance inherent in almost all continuum manipulators causes them to "squeeze" around the perimeter of the continuum contact, evenly distributing the force resulting from even a single degree of freedom of actuation.

The grasp realized using a continuum arm is more qualified by its flexibility (compliance) and this compensates for the lack of accuracy when compared to rigid link robots in positioning the arm to grasp objects.

2.3 CONTINUUM GRASPING - PRACTICE

In this section, we use the results of a series of experiments to demonstrate aspects of continuum grasping (discussed in the previous section) which are easily achievable, and some of which are less accessible at the present time. The experiments discussed below were conducted in the robotics laboratories at Clemson University, using the Octarm VI continuum robot.

The Octarm is a biologically inspired continuum manipulator that resembles an elephant's trunk [29]. Octarm VI has three sections each comprising of three independently actuated pneumatic actuators also known as McKibben actuators positioned at an angle of 120 degrees with respect to each other. These actuators comprise latex tubes (two tubes per actuator in the base and middle sections and one tube per actuator in the tip section) covered with a plastic mesh sheet that is wound in a double helical manner.

When all the three actuators of a section are pressurized with equal amount of pressure, the section extends along the direction of length of the actuator tubes. When the air pressure in one of the actuators is reduced, the section bends with constant curvature. Thus by varying air pressures in the three actuators in suitable proportions, determined by an inverse kinematics mapping procedure [18], the section can be made to bend in different directions having different

curvatures. Thus each section can bend about two axes (x and y) and can extend along a third axis (z) resulting in three degrees of freedom. This gives a total of nine degrees of freedom for the whole manipulator (three per each section) (see figures 2.1 and 2.2).

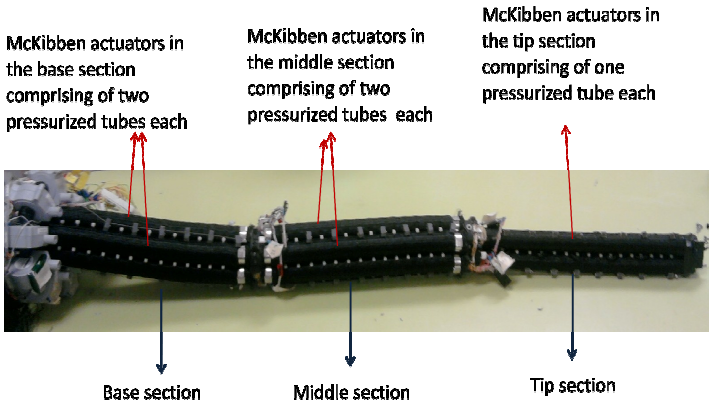

Figure 2.1: Picture of Octarm VI with its three sections and actuators marked

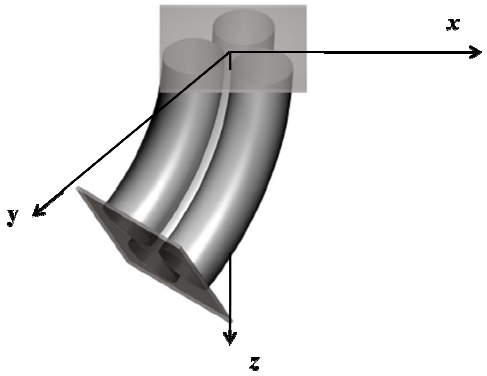

Figure 2.2: Difference in actuator pressures resulting in bending of a section (originally appeared in [31])

Each continuum section of the Octarm has three internal variables – curvature κ, direction of curvature φ, and section length s (see figure 2.3). The forward kinematics of a section of the

manipulator has been developed by approximating each section of the continuum arm by a "virtual" conventional rigid link robotic arm, noticing that the net transformations are the same and then by expressing the conventional D-H table parameters of the virtual robot as a function of the internal parameters of the real manipulator [18]. The homogeneous transformation matrix expressed in terms of the internal variables of the continuum arm is as follows [18],

$$A = \begin{bmatrix} \cos^2\phi(\cos\kappa s - 1) + 1 & \sin\phi\cos\phi(\cos\kappa s - 1) & -\cos\phi\sin\kappa s & \frac{\cos\phi\cos(\kappa s - 1)}{\kappa} \\ \sin\phi\cos\phi(\cos\kappa s - 1) & \cos^2\phi(1 - \cos\kappa s) + \cos\kappa s & -\sin\phi\sin\kappa s & \frac{\sin\phi\cos(\kappa s - 1)}{\kappa} \\ \cos\phi\sin\kappa s & \sin\phi\sin\kappa s & \cos\kappa s & \frac{\sin\kappa s}{\kappa} \\ 0 & 0 & 0 & 1 \end{bmatrix}.$$

From the co-ordinates of the end point of the section, the internal variables can be calculated using the geometry of the section [30]. In such calculations, singularities occur in two configurations – when the curvature is zero and when the tip of the section is at the origin. An inverse kinematics mapping procedure for converting the internal variables (s, κ and φ) of a section to actuator lengths and thereby to air pressures in the three actuators of a section is developed in [18].

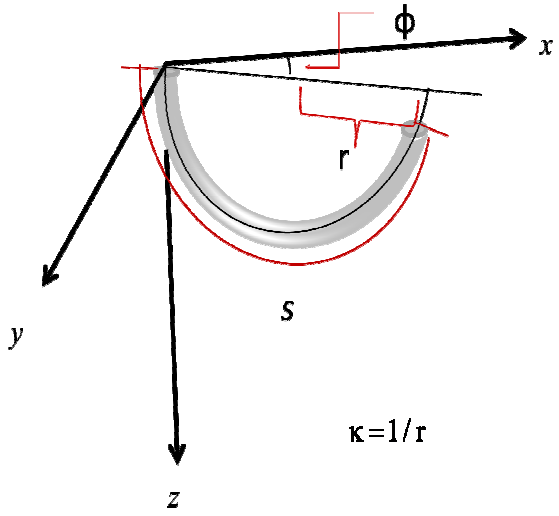

Figure 2.3: Kinematics of a single section of a continuum arm

The fundamental operations of a continuum robot are achieved by the combination of one or more actuator inputs in contrast to conventional rigid-link robots wherein each degree of freedom is controlled by an actuator. With the main motive to make the control of operations intuitive to the operator, the user-interface for Octarm VI has been designed in a way that only the high-level control operation is required from the operator, and obtained as input from a joystick. For a detailed description of various joystick mapping schemes employed to obtain s, κ and φ values of the selected sections from different joystick positions see [30]. The inverse kinematics procedure developed in [18] is implemented to determine the levels of actuator pressures required for the desired position of the arm.

For experiments conducted on continuum grasping and reported on in this paper, the Octarm was placed horizontally on the floor thereby restricting, for each section, one of its degrees of freedom (to bend upwards/downwards). Thus, in such a planar arrangement, each

section can bend sideways and extend along its length; thereby the manipulator as a whole has six controllable degrees of freedom. This arrangement is convenient to analyze grasping of stationary as well as moving objects. Also, maximum curvature for each section is achieved when the Octarm is laid on the floor as bending of the air actuators is not opposed by gravitational effects. Due to mechanical constraints (inherent compliance), some curvature limitation and sagging are unavoidable when the Octarm operates in the spatial (3D) world.

Throughout the experiments on continuum grasping reported here, one or more sections were used and the curvatures were controlled using the joystick. The grasping ability of the Octarm was initially analyzed with a set of stationary objects of different shapes, sizes, textures and orientations. Depending on the size of the object, one or more sections of the Octarm were used for grasping. A firm, continuum contact was observed in grasping spherical and cylindrical objects that aligned with the curvature of the arm. A picture of the Octarm grasping a ball is shown in figure 2.4.

Figure 2.4: Octarm Grasping a spherical object – continuum grasp

While two sections were required to encircle objects having larger diameter, objects were still firmly held by a single section by having a tight grasp, thereby realizing force closure. This is shown in figure 2.5. When more than two sections were used to grasp an object having a circular boundary however, a perfect continuum contact was often not observed as all three sections did not uniformly bend with the same curvature. This can be attributed to the Octarm manipulator's construction which caused all three sections to individually bend with uniform curvatures but not as a whole.

Figure 2.5: Using two sections and one section for grasping the same object

Continuum grasping was exhibited in the case of soft and compliant objects. Compressive forces of the manipulator deform the object and generally distort its boundary to conform to the unloaded shape of the manipulator section. Since the object in this case can comply to a variety of external forces and retain its stability (with respect to position), this kind

of grasp requires the least knowledge of the arm dynamics. However, in the case of objects capable of rolling (like the one described in figure 2.6), it is very important to know the effects of grasp forces on the object. Different contact points and operational speeds of the Octarm can impart different velocities to the rolling object and only a dynamics based strategy can decide the best possible movement for the Octarm to approach and grasp the object without setting it in motion. It was difficult to repeat this experiment with slightly altered initial positions of the object and/or at differing operational speeds of the manipulator.

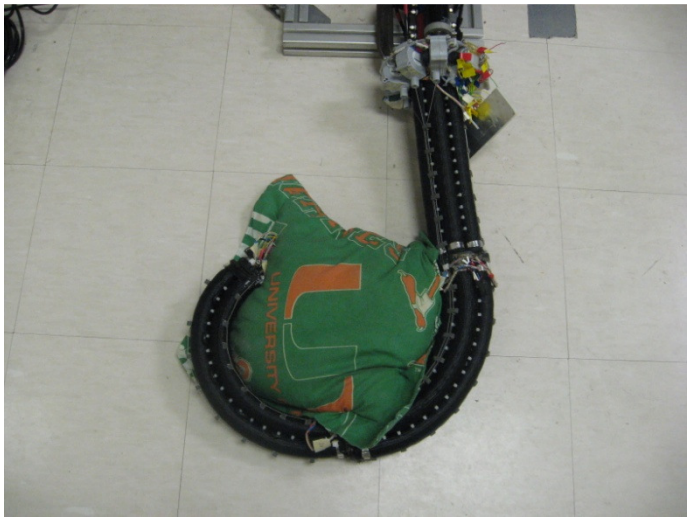

Figure 2.6 Octarm grasping a compliant object

Interesting results were obtained when objects with sharp edges were grasped. While grasping objects of the shapes of cube, cuboid, etc., contacts were made at the edges or at the faces of the object. The number and location of contact points that determined the stability of the grasp were dependent on the initial orientation of the object. Although continuum contact was not possible in this case, the manipulator was able to hold objects through distributed point contacts leading to force closure in the plane (figure 2.7). An increase in tightness of the grasp on

a rigid object flattened the curvature of the manipulator thereby increasing the contact surface area. In these cases, the deformation undergone by the manipulator to successfully hold an object was achieved without knowledge of its mass distribution, compliance and damping properties.

Thus, based on the dimensions, orientation and rigidity of the target object, grasping in practice for fairly simple cases was realized partially by continuum contacts and partially by (locally) point contacts (figure 2.8).

Figure 2.7: Object held by contact points

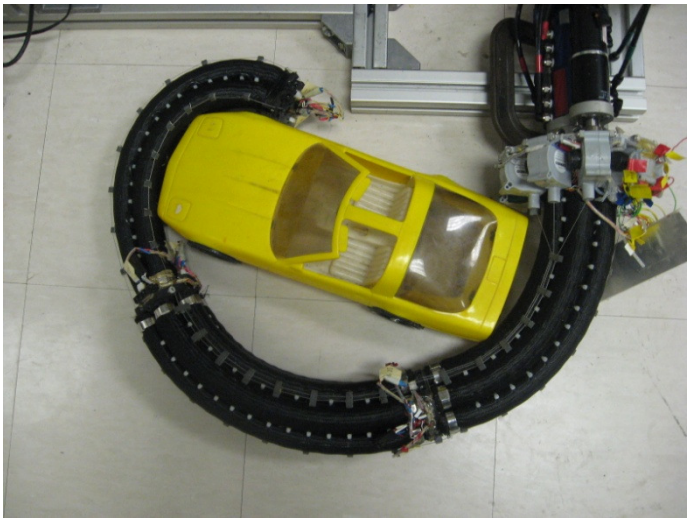

Figure 2.8: Mix of continuum and point contacts

Continuum grasping using the Octarm is particularly attractive in grasping fragile objects (like an egg tray, glass jug) where a soft but firm hold is required (figure 2.9). Potential applications include rescue operations and safe manipulation of delicate objects. Apart from the objects mentioned earlier in this paper, there are also numerous other cases in which a parallel jaw gripper is not plausible. Multifingered robots can provide a more dexterous solution for grasping but at the cost of more complicated mechanisms. Continuum grasping, on the other hand derives inspiration from biological structures and redefines grasping by providing a novel and less complicated approach. Its versatility in handling a plethora of objects makes sense intuitively and is also proven from the above experiments.

Figure 2.9: Grasping fragile objects – using a parallel jaw gripper (unsafe grasp);Octarm

Continuum manipulators also have a potential edge over their competitors via their ability to robustly grasp moving objects without the requirement of precise knowledge of the relative velocity of the moving object. The inherent structure of a continuum manipulator and its nature of grasp are advantageous in grasping moving objects. The Octarm was able to both restrict the motion of and grasp passive but moving objects like a spinning ball, rolling ball and a sliding object as long as the relative motion between object and robot was towards the inner surface of the loop formed by the manipulator (figure 2.10). In the case of passive rolling objects, the grasping was successful for objects that were able to drift and not sufficiently heavy to overcome the momentum of the manipulator. Although a few practical problems were faced due to slow response of the Octarm relative to moving objects, the initial experiments reported here represent the huge potential for grasping non-stationary objects with continuum manipulators. However, a deeper understanding of the manipulator forces (comprising of its inertial, restoring and actuator input forces) is needed to analyze the interaction of the manipulator with non-static objects.

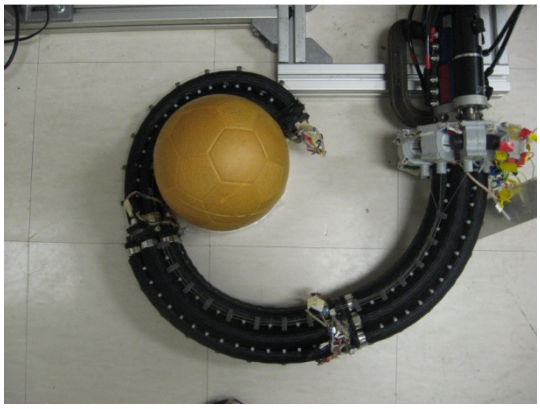

Figure 2.10: Octarm – Grasping and acquiring a moving object

Another topic of interest in this context strongly related to grasping is ‘acquisition’, i.e. restraining and retrieving an object of interest, without necessarily attaining arbitrary influence on the object. Various bio-inspired strategies have been developed to use continuum manipulators to grasp an object and bring it towards the base of the manipulator. This is similar to the behavior seen in animals possessing trunks and tentacles in grabbing food objects. Octopus-inspired strategies developed for the Octarm are explained in [32].

Manipulation of an object grasped is achieved using the base section of the continuum manipulator. Since the Octarm was operated in a plane, manipulation of the base section was restricted to one degree of freedom only in the experiments reported above.

2.4 DISCUSSION

In this section, we analyze the potential of the Octarm to be used for continuum grasping by discussing various aspects of its capabilities as well as a few inherent problems that accompany continuum robot grasping. The analysis is based on quantified physical data and observations made from the experiments outlined in the previous section.

One of the major advantages of any bio-inspired soft robot is its intrinsic compliance which enables grasping of a wide variety of objects whose shape, size and orientation are not accurately known. While holding an object, the continuum arm no longer maintains its constant curvature bending configuration as it deforms to confine to the shape of the object (except for the case of soft and compliant objects in which the object gets deformed). This passive adaptation ability of the Octarm relies on its compliance as well as the rigidity of the object that is being grasped. An approximate measure of the compliances of the three sections of Octarm VI at different levels of actuator pressures, is tabulated below,

Pressure Levels in Actuators (in psi)	Compliance (in 10^{-3} m/Kg)		
	Base Section	Middle Section	Tip Section
12	0.5698	0.5835	1.1454
31	0.3655	0.3699	0.8201
66	0.2776	0.2876	0.5705
80	0.2276	0.2302	0.4262

Table 2.1: Compliance of all three sections (measured in a direction perpendicular to the length of the arm

The compliances of the base and middle sections are almost identical. The tip section, having a thinner structure than the other two sections, is more compliant. With an increase in actuator pressure, the stiffness of each section increases thereby making it less compliant.

There are a few potential problems faced with the operation of the Octarm in full 3D environments which degrade its performance in grasping to certain extent. A comparison of the approximate curvatures of the three sections of the Octarm VI measured in planar (2D with the effects of gravity eliminated) and in 3D configurations is given below.

Section	Maximum Curvatures (in m^{-1})	
	Planar (2D operation)	Spatial (3D operation)
Base Section	3.98465	2.28228
Middle Section	4.16693	3.79449
Tip Section	8.33072	8.07598

Table 2.2: Approximate curvature of sections

The maximum curvatures of the three sections in 3D configuration are less than the ones achievable in 2D planar configuration. The maximum curvatures that can be achieved also give an idea of the dimensions of the object that can be effectively grasped using one or more sections of the Octarm.

In 3D operation, the manipulator's position deviates slightly from its predicted kinematics which can be largely attributed to sagging effects due to gravity and weight of the arm. Also, when the manipulator carries and lifts objects, its ability to grasp is limited by the payload capacity of the arm. The maximum load which the Octarm VI can sustain without deforming its grasping configuration is given below.

Weight of Octarm VI (approx.)	6.93996 Kg
Payload (lifting against gravity)	0.90718 Kg

Table 2.3: Payload of the Octarm

The time taken for each section to expand to its maximum possible length, i.e for the pressure in the actuators to increase from 0 psi to a maximum value (80 psi) is given in table 2.4. Currently, there is no explicit mechanism to regulate the speed of operation of the Octarm. However, faster movement of the Octarm for the same curvature can be observed by varying at maximum section length (s).

Section	Time taken for the pressure levels to increase from 0 psi to 80 psi in all the actuators (in seconds)	maximum percentage of extension
Base section	5.51	27.18
Middle section	5.66	42.47
Tip section	5.78	38.5

Table 2.4: Actuator parameters

Although 3D operation of the manipulator permits an infinite number of directions of bending for grasping, the inherent design of the manipulator permits maximum curvature to be achieved only three directions (ϕ =30°, 150°, 270°) when the section bends away from any one of its three actuators. Also, there is a second local maximum curvature that can be achieved along three directions (ϕ = 90°, 210°, 330°) when the section bends away from any two of its three actuators. This imposes a restriction on effective grasping operation of the arm in spatial configurations. For the experiments conducted in planar 2D space, the Octarm is bent along the direction of maximum curvatures. The curvature values of each section reported in this chapter also correspond to the directions of maximum curvatures.

In this chapter, we have discussed and demonstrated the potential of continuum robots in grasping via a series of experimental case study examples. However, as illustrated in the experiments, numerous challenges need to be addressed before under-actuated continuum grasping becomes a practical option. There is a significant difference between the kinematic parameters that are given as input to the system (through the joystick) and the actual shape parameters evinced from the arm's configuration. This effect is more pronounced in 3D operations of the manipulator. The current controller implementation is based purely on the arm's kinematics and hence it does not account for the various internal and external forces acting on the arm. The omission of the effects of masses inherent the physical construction of the arm and gravitational effects are examples of several modeling defects which hinder the arm from exhibiting a behavior as predicted by existing kinematic (i.e. purely geometric) continuum arm models. This is true even for non-contact motion of the robot. In the context of grasping, there are additional grasp forces involved when an object comes in contact with the manipulator. The

interaction between the dynamics of the continuum arm and that of the object through the grasp forces are yet to be defined and modeled in the literature. A knowledge of the system dynamic forces (a combination of the actuating and restoring forces, and the system dynamics which create them) will help in optimizing grasp points and strategies for different classes of objects, determining the speed of operation of the arm, analyzing the capabilities of the arm to acquire (for example) a moving object of given velocity and direction. A dynamic analysis will also have a major influence in segregating objects that can be grasped based on their shape, dimension and weight when it comes to spatial operation in which gravity plays a significant role. Dynamics-based algorithms for determining optimal grasp points/grasping configurations for grasping general classes of objects will be critical in planning practical strategies for Continuum Grasping. In Chapter 4, in order to begin to address the above issues and concerns, we introduce a new approach to practical dynamic modeling for continuum robots. As a necessary precursor to that approach, in the following chapter we characterize the actuators which comprise the underlying inputs for the dynamics of continuum robots.

CHAPTER THREE

EXTENSOR MUSCLE CHARACTERIZATION

3.1 LITERATURE REVIEW

The common objective of most of the Continuum Robots built so far is to mimic the physical formation and operation of continuous actively movable biological structures. Although various construction techniques to realize a physical Continuum Robot have been proposed and implemented, the preferred approach in the literature thus far is to build a continuum structure using actuators that resemble a biological muscle in functionality. McKibben actuators a.k.a air muscle actuators form the backbone of Octarm VI and two of its previous generation prototypes. The positioning of these air muscles determine the robot's actuated degrees of freedom (that can be directly controlled when it is being operated). A brief description of how these muscles contribute to the basic movements of Octam VI by controlling the pressures in each of the McKibben actuators that make up the arm was presented in Chapter 2.

A picture of a typical McKibben actuator is shown in figure 3.1. It consists of a latex tube enclosed within a fully compressed (lengthwise) braided sleeve. The ends are sealed with brass terminals. One of the terminals has a provision for fitting an adapter that is connected to the pressure lines. The other terminal is a stopper. See figure 3.2 for a picture of the actuator components.

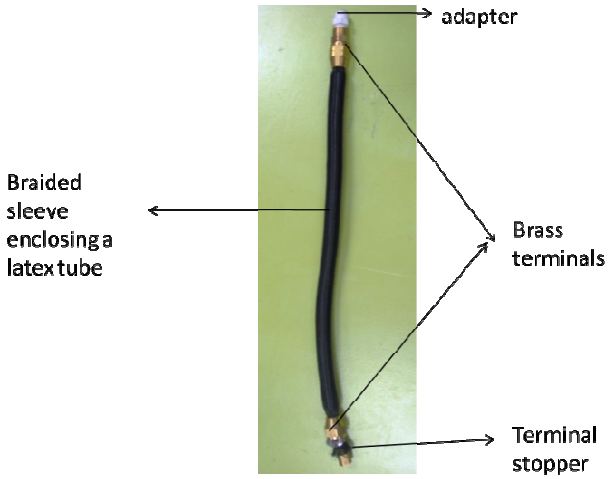

Figure 3.1: McKibben actuator

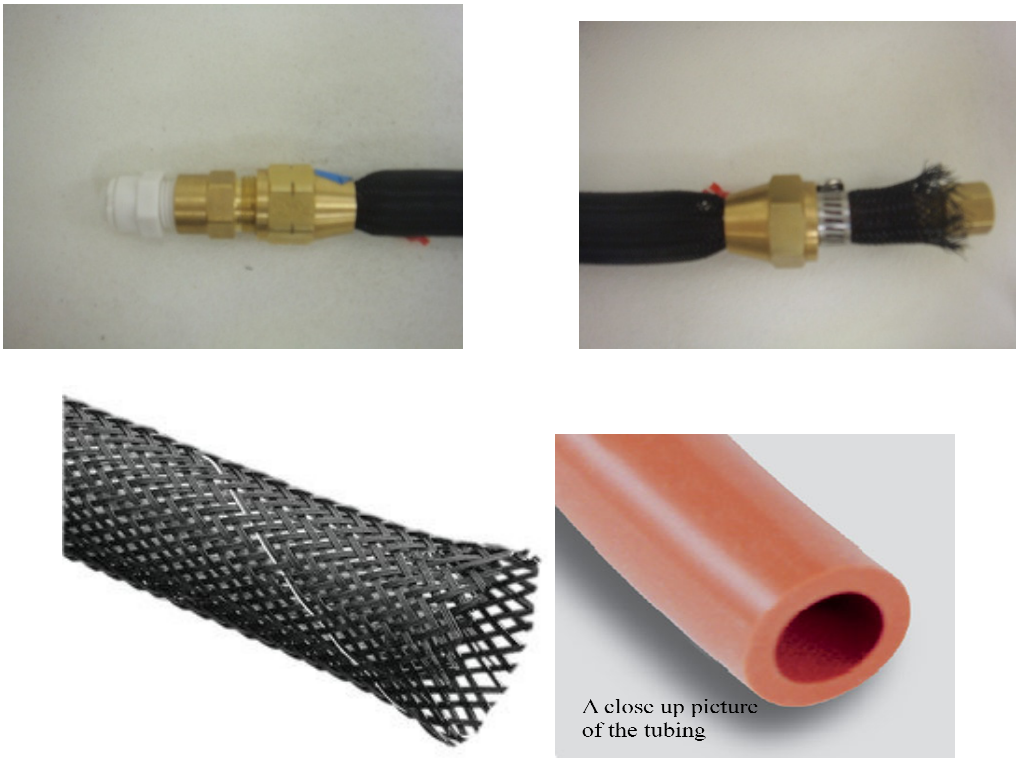

Figure 3.2: Components of air muscles

Notice that, unlike the case of conventional rigid link robots, for continuum robots based on McKibben muscles, the robot (and thus inherently its dynamic properties) is to a large extent dominated by its actuators. Note that for conventional rigid link manipulators, actuator dynamics are usually either an "add-on" to rigid-link dynamical models, or omitted entirely [21]. This is due to the fact that the transmissions –usually high-ratio gearing – between the actuators and mechanism (links) significantly attenuates the dynamic effects of the actuators in conventional robots. This is not the case for continuum robots whose body largely comprises the actuators, and there is no transmission as such. Thus in analytical modeling of McKibben actuator-based Continuum Robots, the dynamics of the actuators should be incorporated as an inherent part of the dynamics.

A useful actuator model should model the force exerted by the actuator as a function of input pressure. The effects of extension/compression of the braid and expansion of the latex tube need to be modeled to derive a suitable expression relating force and pressure. Some work in modeling McKibben muscles has appeared in the literature, and the main resulting actuator models are summarized in the following paragraphs.

Chou and Hannaford were the first to develop a model for McKibben actuators [33]. They approximated the actuator's shape by a cylinder and expressed the length of the actuator (L) and length of one thread in the braid (b) as a function of the braid angle (ψ). See figure 3.3 for the actuator parameters. By equating the work done by the input pressure and the work done by the actuator force, an expression relating force and input pressure (relative to the atmospheric pressure) is obtained.

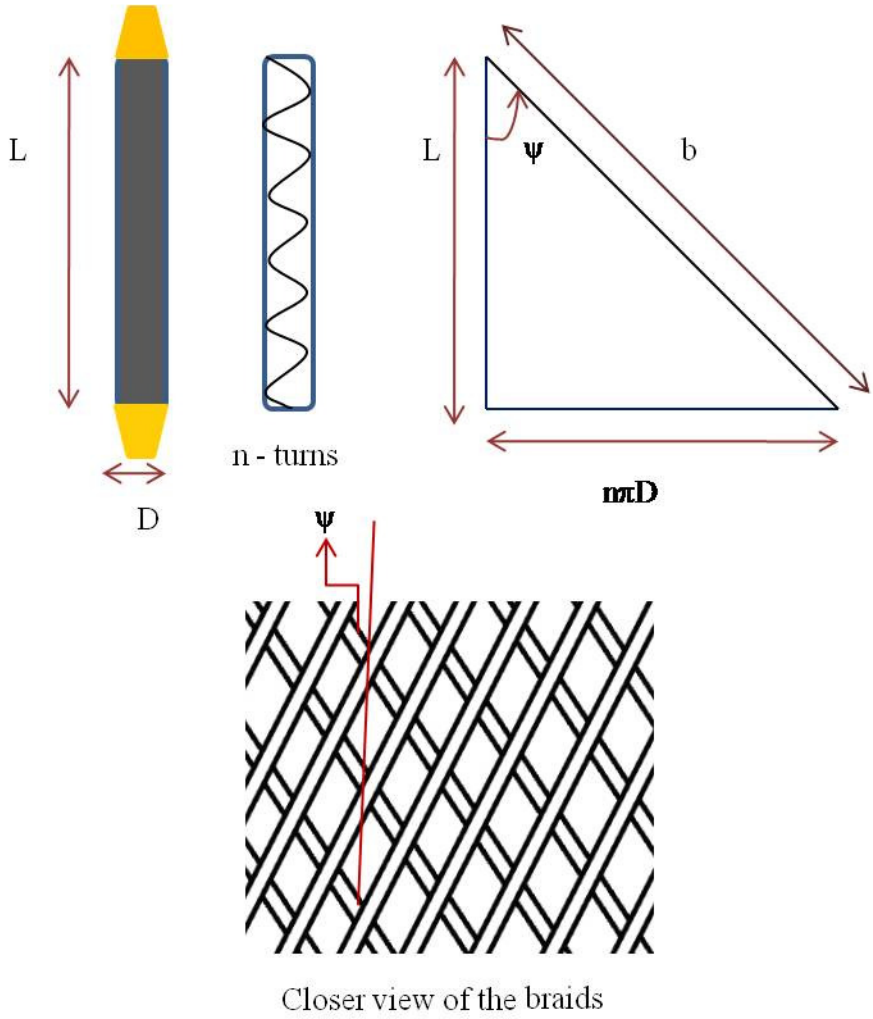

Figure 3.3: Actuator model

The actuator parameters and variables as illustrated in [2] are:

L – Length of the actuator

D – Diameter of the actuator

n – Number of turns of thread

b – Thread length

ψ - Braid angle.

Of the quantities introduced above, b and n are constants. The variables ψ and D vary inversely with increase in L. The importance of braid angle will be discussed later in this chapter.

$$L = b\cos\psi \tag{3.1}$$

$$D = \frac{b\sin\psi}{n\pi} \tag{3.2}$$

Equating the internal and external work done in the actuator,

$$-FdL = P'dV \tag{3.3}$$

where F is the actuator force and P' is the relative pressure. In the above equation V is the volume of the cylinder (actuator model) and is given by

$$V = \frac{1}{4}\pi D^2 L. \tag{3.4}$$

Differentiating V and L with respect to ψ and substituting the result in the energy conservation equation, an expression for actuator force is obtained:

$$F = \frac{P'b^2(3\cos^2\psi - 1)}{4\pi n^2}. \tag{3.5}$$

The above equation models the basic functionality of air muscles representing the effects of variation of braid angle, actuator length and diameter on force. However, the friction effects due to expansion of the latex tube and braided sleeve are not considered in the above model.

Chou and Hannaford extended their above model further by adding an additional term in the force expression by taking into account the thickness of the inner latex tube [34]. The accuracy of the model was improved in [35] by adding a non-linear, Mooney-Rivlin model of the inner tube. The work presented in [36] consists of characterizing the experimental behavior of McKibben actuators of different dimensions, braid angles and diameters. The authors of [36] have also proposed an increased accuracy model that includes elastic energy effects of the latex tube and braids, non–cylindrical shape and variable thickness. Muscle characterization is also presented in [37] in which a hexapod platform is built using McKibben actuators. A more detailed description of the actuator's concept, operation, properties, classification and application is given in [38] and [39]. In [40] a hybrid of the McKibben actuator is built by impregnating the braids with SMP (Shape Memory Polymer) resin. This will help the actuator to remember its shape, thereby potentially eliminating the need for continuous control.

Other applications in which McKibben actuators have been used are prosthetic arms and hopping robots. Note that in each of these cases it is strongly desired, if not essential, to have a device that mimics (biological) muscle movements. A detailed description of a possible implementation model of a hopping robot using McKibben actuators is given in [41]. The presentation in [42] describes the modeling and control of a walking robot which has McKibben actuators connected in an antagonistic pair configuration.

3.2 CONTRACTORS AND EXTENSORS

The previous work described above is a useful starting point in building models for continuum robot actuators. However, there is a fundamental difference between the McKibben actuators used and modeled previously and those required in continuum robots. The McKibben actuators that have been modeled and characterized so far are termed contractors. This is because they replicate the functionality of a biological contractor muscle – a muscle that contracts when activated and elongates when it is relaxed. Similarly, when a contractor artificial muscle is pressurized, the volume of the inner tube tends to increase, but due to the high longitudinal stiffness of the braids, the braids increase in diameter and shorten in length. Thus the ends of the actuator are pulled together by the contracting braids.

However, another type of artificial muscle, dual to the contractor type thus far analyzed in the literature, is more appropriate for continuum robots. It is quite feasible to analyze and construct another kind of air muscle having the reverse operation to contractors. These are termed extensors and are the type being used (but not thus far mathematically modeled) in continuum robots. As may be inferred from the name, these muscles extend when pressurized. The braids in an extensor prevent lateral extension of the actuator and allow longitudinal extension. The braid pattern for both extensors and contractors are essentially the same; it is however the braid angle which determines the actuator type. For braid angles greater than 54.7 degrees, the actuator behaves like a contractor and vice versa. This property is analogous to that of fibre angles in biological muscles [43]. Hence the force exerted by a contractor on an external load is a pulling force and that exerted by an extensor is a pushing force.

3.3 EXTENSOR CHARACTERIZATION

In this section we present a model for extensor air muscles. The model is, to the best of our knowledge, the first analytical model for extensor air muscles, and represents one of the main contributions of this thesis. The core underlying model considered for deriving the actuator force expression for extensors is same as the one developed by Chou and Hannaford. The physical structure of extensors is same as contractors and the cylindrical approximation of the inner tube holds good in this case too. (The same expression for L and D as a function of ψ can be used). However, there are also key differences. The direction in which force is defined is reversed. Since the direction of actuator force is same as the direction of change in length, the negative sign in the energy conservation equation can be removed. The resulting force expression is

$$F = \frac{P' b^2 (1 - 3\cos^2 \psi)}{4\pi n^2}. \tag{3.6}$$

By observing the expressions above, we note that the force is a function of pressure and braid angle. Although there are two variables in the system, namely L and D, the change in configuration is represented by one system variable (ψ). For a given pressure, the braid angle can be varied by varying the load at one of the actuator ends. For a given pressure, a contractor exerts maximum pulling force when its contraction percent is zero (at maximum length). Analogous to this, the extensor exerts maximum pushing force when its extension percent is zero (at its minimum length). While the maximum possible force exerted by both types of muscles depends on their original braid angle, both the actuators have zero force when their braid angle is

54.7 degrees. (This is the angle obtained when the actuator force expression is differentiated with respect to ψ and equated to zero.) The expression can be written as follows after replacing the cosine term with L and b

$$F = \frac{P'b^2}{4\pi n^2}\left(1 - \frac{3L^2}{b^2}\right). \tag{3.7}$$

The above expression represents a new analytical model for extensor air muscles. It has potentially highly significant importance via application in continuum robot dynamic models, if validated against the appropriate hardware. Next, we present and detail the results of experiments conducted to validate the above expression. The actuator set up is shown in figure 3.4. An extensor air muscle actuator was clamped at one end and its other end was pressed against a digital weighing scale. The actuator was enclosed in a plastic tube that prevented buckling of the actuator when its length was constrained.

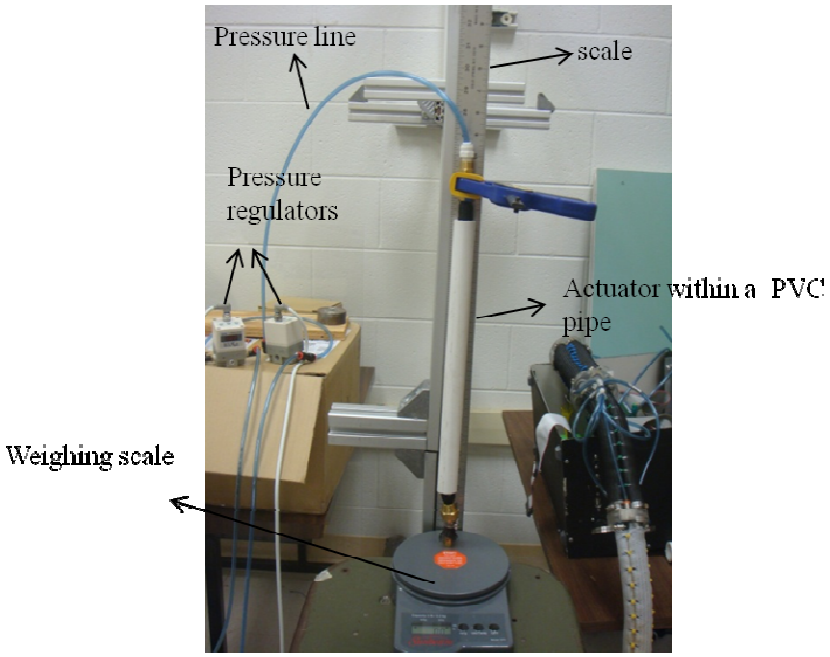

Figure 3.4: Actuator characterization

The pressure level of the actuator was varied using a commercial pressure regulator (one of the two shown in Figure 3.4 was used). The weighing scale readings were converted to force measurements. The following graph is a plot of measured and calculated values of force at different pressure levels when the extension percentage of the actuator was zero (zero displacement). The corresponding values are given in Table 3.1.

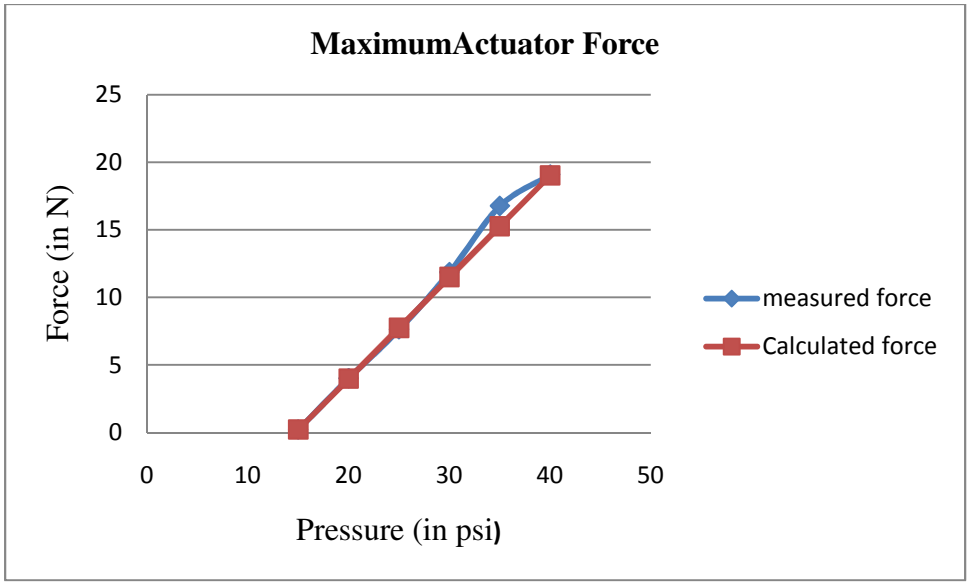

Figure 3.5: Actuator forces at zero extension

Pressure level (in psi)	Measured Force (in N)	Calculated Force (in N)
15	0.232	0.226
20	4.018	3.986
25	7.629	7.746
30	11.858	11.506

35	16.758	15.266
40	19.081	19.026

Table 3.1: Actuator forces at zero extension

The forces at the actuator's original length (zero extension) are seen to be very close to the values predicted by the model. However, there was a significant variation between the forces predicted by the model and the measured forces when there was extension (The actuator was allowed to extend to different levels by slowly releasing its clamp and re-clamping at slightly displaced positions on the top.) Refer to Appendix A for details on how the muscle parameters and hence the forces were calculated.

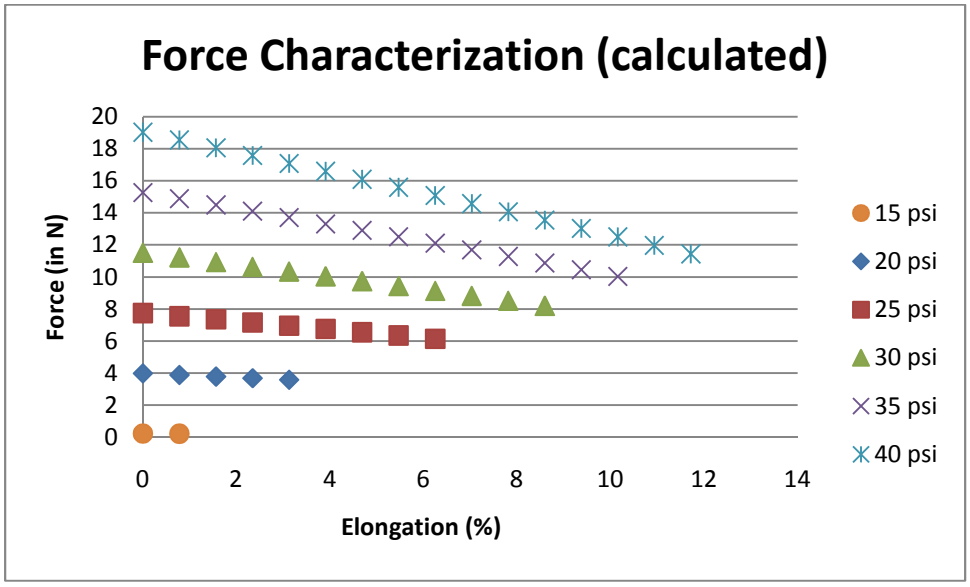

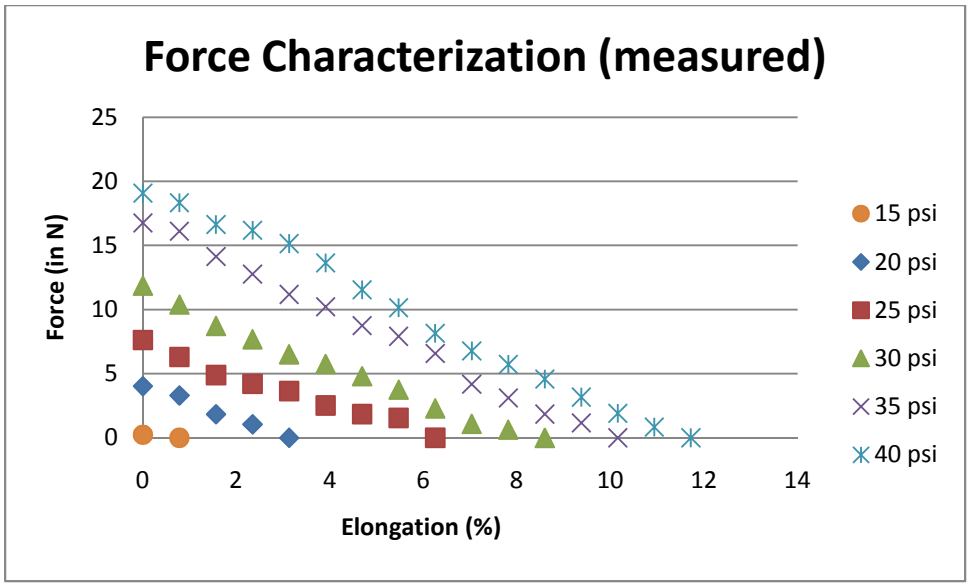

Figure 3.6: Actuator forces at different % of extension

The model predicts the forces to become zero at a specific length. However, it is observed that the actuator's length does not extend beyond a certain limit for a given pressure level. We explain the discrepancy as follows. The force expression derived in line with the model developed by Chou and Hannaford for contractors considers substantial functional aspects of the physical muscles but omits a few other behavioral aspects associated with the tubing and the sleeve of the actuator (e.g, the response of the tube and sleeve to the various internal frictional forces) which explains why the actual muscle does not follow the trend predicted by the model. For the Continuum section dynamic model developed in the following Chapter, we have adopted a second order interpolating polynomial of experimental force data (at different pressure levels) for the actuator forces. The force polynomial at a given pressure level is a function of the length of the section. A plot of the experimental force data and the interpolating polynomials for different pressure levels for the experiment discussed above is shown in figure 3.7.

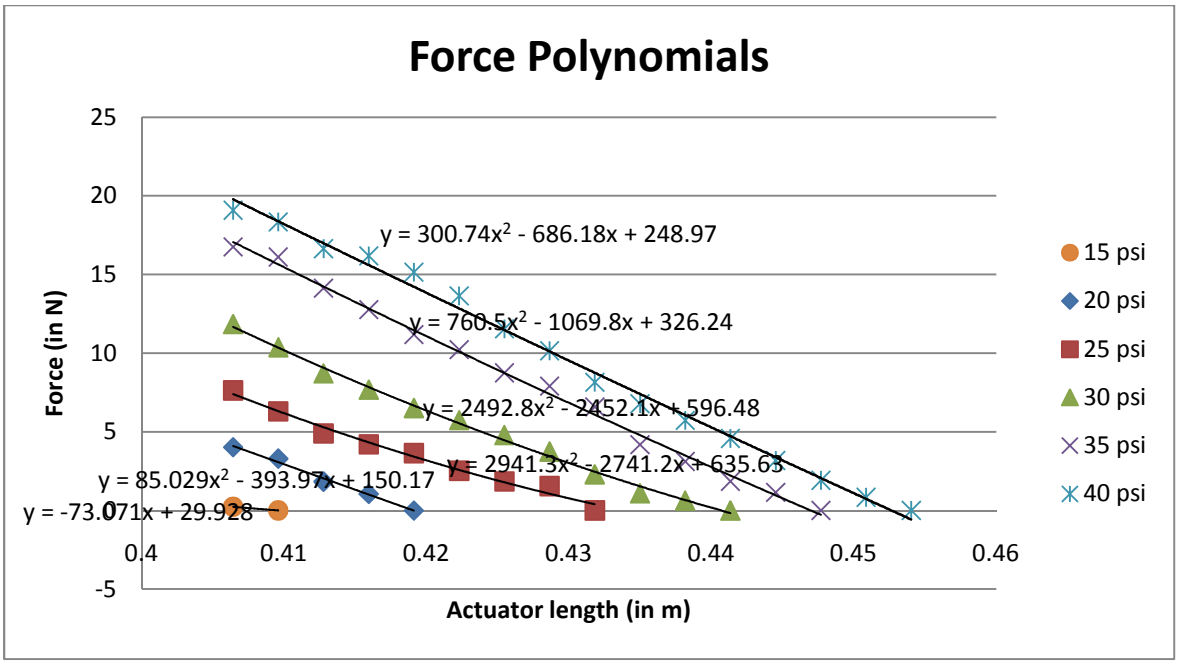

Figure 3.7: Interpolation of experimental actuator force data

For 15 psi, the actuator force was nearly zero and it was not possible to measure forces at more than one position at that scale. Therefore, the force polynomial for 15 psi is of order 1.

In the case of the Octarm and the continuum arm prototype (that was built to validate the dynamic model explained in chapter 4), the diameter of the actuator is nearly a constant throughout the working range of pressures. The diameter change of the actuator is not visibly apparent but there is approximately a 0.1mm decrease when the pressure is changed from 15 psi to 65 psi. Based on this fact, another simplified expression for actuator force has been proposed. This is derived based on the principle of virtual work and the assumption of constant diameter has been included in this model. According to the principle of virtual work, for an extensor muscle,

$$FdL = P'dV. \tag{3.8}$$

The diameter of the actuator is nearly a constant and the actuator's shape is assumed to be cylindrical. Therefore the change in volume can be written as

$$dV = \pi D^2 dL. \tag{3.9}$$

Hence, the actuator force is given as

$$F = \pi D^2 P'. \tag{3.10}$$

The results and implications of using this model and the former in continuum manipulator dynamics will be presented and discussed in chapter 4.

Having proposed two different methods to characterize the extensor force, next the characterization of another key parameter of an air muscle is explained. In the dynamic model presented in the next chapter, we will see that the stiffness of the actuator is modeled as a spring element. The experimental values of stiffness of the actuators are ultimately substituted for the stiffness constants of the springs. The stiffness of the actuator varies with pressure levels and is experimentally determined by a simple load test. Since we used a pair of McKibben muscles coupled along their length using zip ties as the prototype of a continuum arm section, the load test was performed on this rather than a single muscle. From a stiffness perspective, the prototype thus mentioned corresponds to two springs connected in parallel, thus, the stiffness of one muscle can be deduced to be one-half of the stiffness measured from the experiment. The actuator pair was loaded in steps of 1 pound increments at its lower end (with its upper end clamped) and the corresponding displacements were measured. The force-displacement

relationship is approximately linear and the slope of the line fit to the data by least squares method is taken as the value of the stiffness constant. The increase in stiffness with pressure is close to linear and a least square curve fit is used to calculate the stiffness constant at various actuation levels in the model. Note that in the first plot, the forces correspond to the actuator pair.

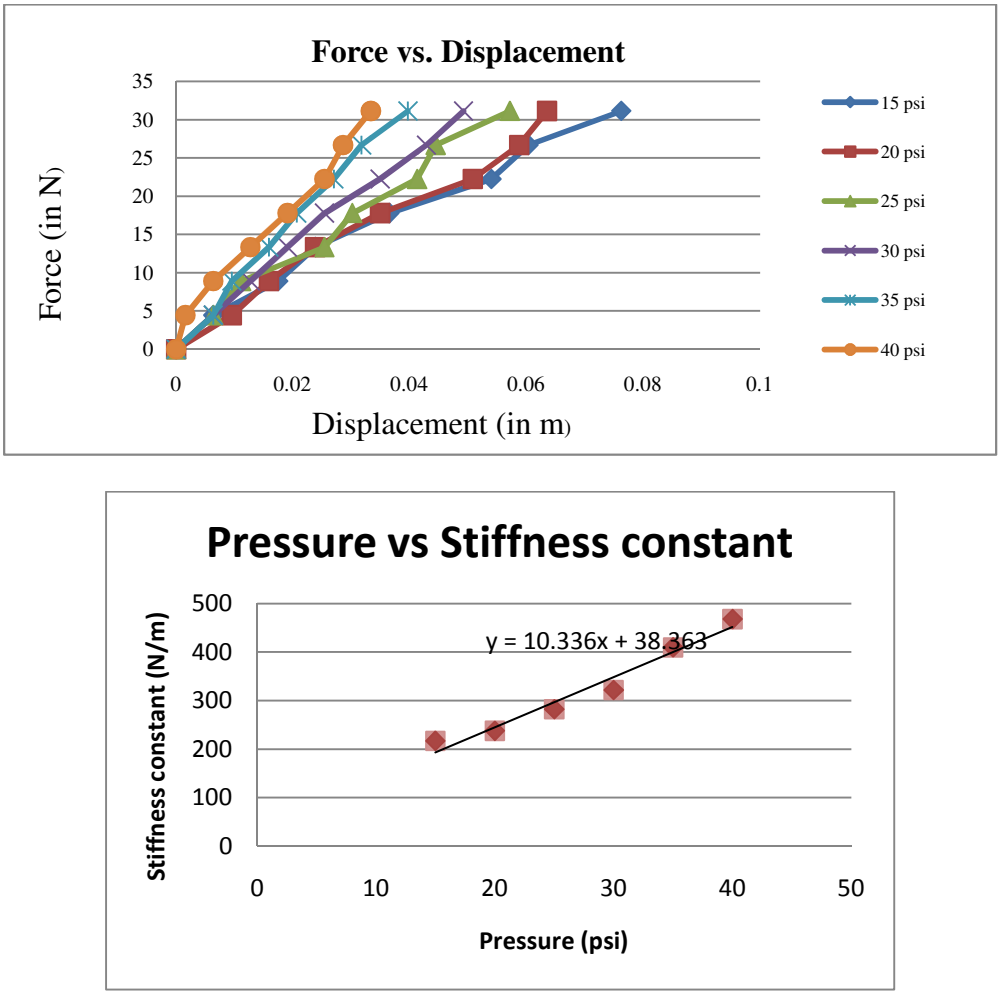

Figure 3.8: Stiffness characterization

In this chapter, new theoretical actuator force models and empirical determination of the actuator stiffness constant were described in detail. It was seen that the basic theoretical force model does not include all possible muscle behaviors. The more detailed and closer approximating models (for contractor muscles) proposed in [34], [35] and [36] have complex expressions that are difficult to integrate in dynamic models, and hence extending the basic extensor muscle model along those lines is not attractive given the overall aims of this thesis. The new work presented in this chapter on modeling extensor McKibben muscles and extensor force characterization, while sufficient for our goals of developing continuum robot dynamics in the next Chapter, is only the beginning. The task of detailed theoretical modeling of extensor muscles remains an independent topic which we suggest could be productively be focused on by other researchers in the near future. However, in subsequent work in this thesis, we apply two force models; one using interpolating polynomials based on experimental data, and the other based on the constant actuator diameter approximation giving a force expression which is not a function of the actuator's length.

CHAPTER FOUR

EFFICIENT LUMPED PARAMETER DYNAMIC MODEL OF A CONTINUUM ARM SECTION

4.1THE PROBLEM AND MOTIVATION

In this chapter, a new dynamic model is proposed for a section (the key structural element) of a Continuum Robot Arm. The core content of this chapter consists of the derivation of the analytical model. The underlying need for a dynamic model to help in understanding the operation of a Continuum Robot in a real world scenario has been presented in Chapter 2. This chapter concentrates on modeling principles and techniques required to circumvent the cumbersome process involved in following existing proposed mathematical techniques for developing the full dynamics of a Continuum structure. The constraints introduced in the model herein to match the physical model of Octarm VI supported by the results of numerical simulation are also presented. The core results of this chapter will be presented in [66]

With the establishment of fairly general kinematic models of Continuum Robots in the past decade or so, more recently researchers in this field are actively focusing on the development of analytical models to analyze continuum arm dynamics. The first approach to this was proposed by Chirikjian, albeit based on an infinite degree of freedom model [44]. In [45], Newton Euler equations along with a Cosserat beam model were used to model the dynamics of an eel-like robot. Later, 3D position tracking and motion control with feedback for the eel-like robot were also developed [46]. Also based on Cosserat theory of elastic rods, a non-closed form,

geometrically “exact” model was developed in [47]. A novel method of modeling planar motion of snake-like robots using virtual work principles and by the addition of a nominal mechanism for a snake-like robot body is presented in [48]. A detailed account of closed-form Lagrangian dynamic models for continuum robots is introduced in [49], [50] and [51]. The Continuum Robot was modeled as a parameterized curve and energy functions were integrated along the length of the curve. Tatlicioglu’s work ([50] and [51]) extended the model developed by Mochiyama and Suzuki [49] for Continuum Robots to include extensibility as an additional degree of freedom. While Tatlicioglu’s work utilized a geometric model of a Continuum Robot, the dynamic model presented in this thesis uses a linearized model of the actuators as the building blocks of the section’s model. However, from the point of view of practice, the fundamental theoretical approach of modeling full continuum arm dynamics based on classical or continuum mechanics is not favorable due to the magnitude of complexity of the resulting models. There is a pressing practical need to adopt a completely different modeling scheme and/or to introduce sufficient assumptions in the model which will make its realization in real robot hardware feasible, possibly with an acceptable compromise in its accuracy.

The work illustrated in this thesis derives inspiration from modeling of biological segments using discrete mechanical elements [52],[53]. The principal modeling idea is to slice a continuum structure into a finite number of similar modules and represent each module using simple lumped parameter elements. This model will be seen to be quite effective, at the cost of retention of some complexity issues. Useful features of the approach and issues impeding further development are discussed in later sections of this Chapter.

4.2 MODELING PRINCIPLES

This Chapter is primarily intended to forward the study of dynamics of general continuum robots. To ground the results on real hardware, the model herein is focused on the Octarm VI continuum robot. Hence, the parameters and constraints implemented in this model conform to that of Octarm VI. Since each section bends in space to form a constant curvature section its analysis can be restricted to a plane during these movements (the orientation of the plane changes as the robot moves). Therefore, a planar model is effective for the case of a single continuum robot section, the subject of the analysis in this Chapter. From the Octarm's three shape-defining parameters, s, κ and φ, in the 2-D single-section case now under consideration, orientation (φ) can be neglected. Two coupled actuators are sufficient to model planar operation of a single-section of a continuum arm. We model each actuator as a Mckibben (extender) actuator, as realized in the Octarm hardware. The inherent compliance and damping of each actuator will be represented as a linear spring and damper combination. Thus each module in the model has a pair of linear spring and damper struts. The actuators maintain an almost constant diameter at all pressure levels and this is accounted for in the model by constraining the distance between the two spring and damper struts. The length of arc (s) of each module is the average length of the two actuators. Another parameter, θ, is introduced to account for bending such that $\frac{1}{\kappa} = \frac{s}{\theta}$.

Figure 4.1: Octarm VI, individual actuators and planar equivalent prototype

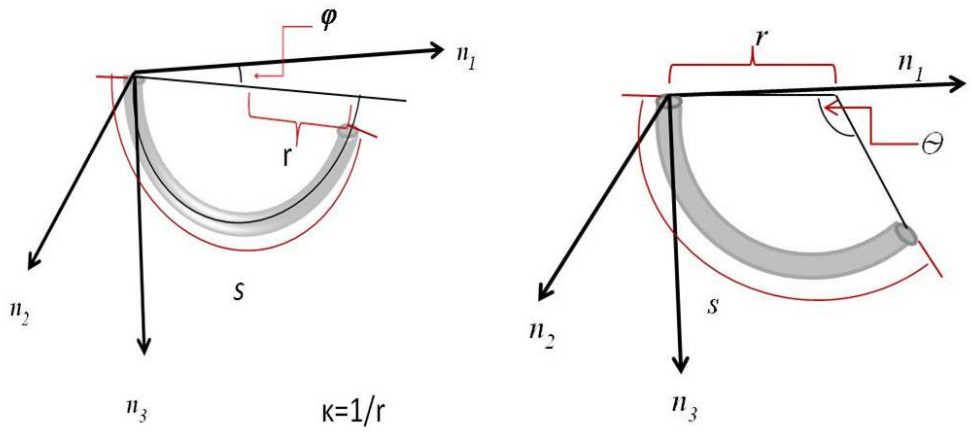

Figure 4.2: Parameters in spatial and planar configurations (originally appeared in [54])

4.3 DERIVATION OF THE THREE-MODULE MODEL

The Continuum section analytical model developed here consists of three modules stacked together in series. In general, the model will be a more precise replication of the behavior of a continuum arm with a greater of modules included in series. However, we will show that

three modules effectively represent the dynamic behavior of the hardware, so more complex models are not motivated.

The generalized co-ordinates in the system are,

s_i, θ_i for i=1,2,3.

The subscript i denotes the module number. The first coordinate represents the extension of each module and the second coordinate signifies the change in orientation of the (assumed) rigid rod connecting the two actuators.

The generalized forces corresponding to the generalized co-ordinates are

Q_{s_i}, Q_{θ_i} for i=1,2,3.

There is a generalized force and a generalized torque in the system which impart a linear velocity and an angular velocity, respectively. In other words, the force directly produces extension of the arm and the torque directly causes the section to bend. The forces F_{1i},F_{2i} for i=1,2,3 represent the input forces due to air muscles in the system. The underlying models for derivation of these actuator force expressions have already been synthesized in chapter 3. Since air-pressure is assumed uniform throughout the entire length of each of the actuators, the corresponding input forces acting in all the three modules should be same. Thus, the constant curvature bend exhibited by the section is incorporated inherently within the model.

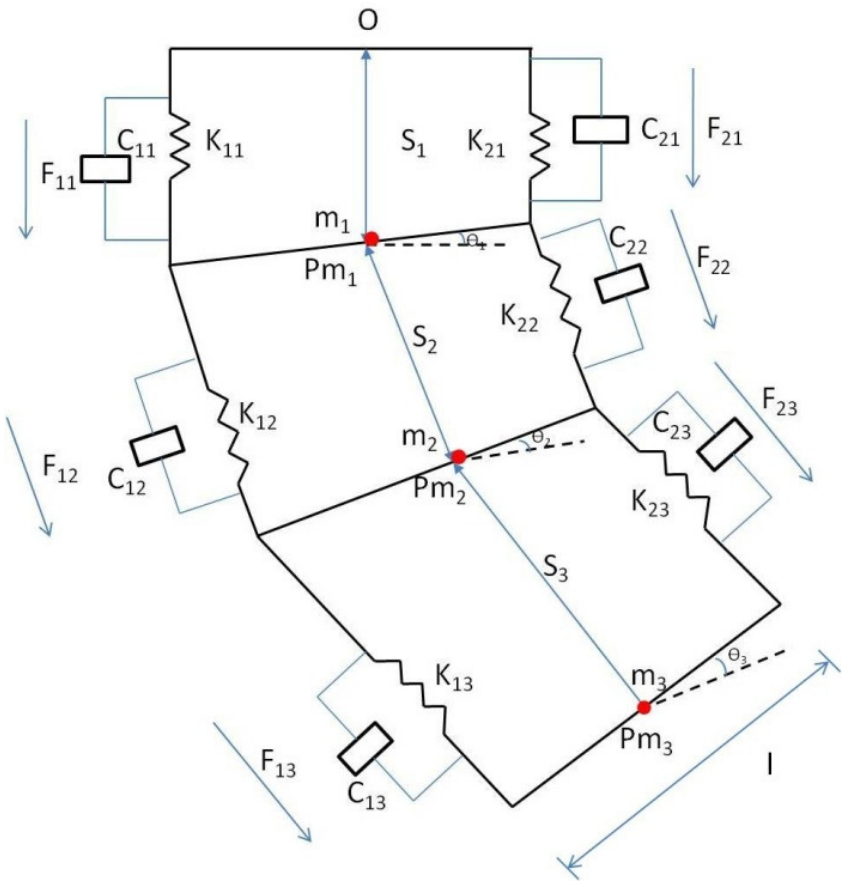

Figure 4.3: Assumed structure for analytical model of a section of a continuum arm

The other model parameters are,

l- Length of the rigid rod connecting the two struts, constant throughout the structure

k_{1i}, i=1,2,3 - Spring constant of actuator1 at module i

k_{2i}, i=1,2,3 - Spring constant of actuator2 at module i

c_{1i}, i=1,2,3 - Damping coefficient of actuator1 at module i

c_{2i}, i=1,2,3 - Damping coefficient of actuator2 at module i

m_i, i=1,2,3 - Mass in each module

I_i, i=1,2,3 - Moment of inertia of the rigid rod in each module.

The mass of the arm is modeled as being concentrated at three points whose co-ordinates referenced with respect to. a global inertial frame (N) located at the base of the arm are given below (see figures 4.2 and 4.3),

$$^{N}P_{m_1} = s_1 \hat{n}_3 \tag{4.1}$$

$$^{N}P_{m_2} = s_2 \sin\theta_1 \hat{n}_1 + (s_1 + s_2 \cos\theta_1) \hat{n}_3 \tag{4.2}$$

$$^{N}P_{m_3} = (s_2 \sin\theta_1 + s_3 \sin(\theta_1 + \theta_2)) \hat{n}_1 + (s_1 + s_2 \cos\theta_1 + s_3 \cos(\theta_1 + \theta_2)) \hat{n}_3. \tag{4.3}$$

The position vector of each mass is initially defined in a frame local to the module in which it is present. These local frames are located at the base of each module and oriented along the direction of variation of coordinate 's' of that module. The rotations and the translations between the local frames and the base frame (located at point O) are given in appendix B. The positioning of each of these masses is at the centre of mass of the rigid rods connecting the two actuators.

Differentiating the position vectors we obtain the linear velocities of the masses. The kinetic energy (T) of the system comprises the sum of linear kinetic energy terms (constructed using the above velocities) and rotational kinetic energy terms due to rotation of the rigid rod connecting the two actuators, and is given below as

$$T=(0.5)m_1\dot{s}_1^2+(0.5)m_2((\dot{s}_2\sin\theta_1+s_2\cos\theta_1\dot{\theta}_1)^2+(\dot{s}_1+\dot{s}_2\cos\theta_1-s_2\sin\theta_1\dot{\theta}_1)^2)+(0.5)m_3((\dot{s}_2\sin\theta_1 +s_2\cos\theta_1\dot{\theta}_1+\dot{s}_3\sin(\theta_1+\theta_2)+s_3\cos(\theta_1+\theta_2)\dot{\theta}_1+s_3\cos(\theta_1+\theta_2)\dot{\theta}_2)^2+(\dot{s}_1+\dot{s}_2\cos\theta_1-s_2\sin\theta_1\dot{\theta}_1+ \dot{s}_3\cos(\theta_1+\theta_2)-s_3\sin(\theta_1+\theta_2)\dot{\theta}_1-s_3\sin(\theta_1+\theta_2)\dot{\theta}_2)^2)+(0.5)I_1\dot{\theta}_1^2+(0.5)I_2(\dot{\theta}_1^2+\dot{\theta}_2^2)+ (0.5)I_3(\dot{\theta}_1^2+\dot{\theta}_2^2+\dot{\theta}_3^2). \quad (4.4)$$

The potential energy (P) of the system comprises the sum of the gravitational potential energy and the spring potential energy. A small angle assumption is made throughout the derivation. This allows us to directly express the displacement of springs and the velocities associated with dampers in terms of system generalized coordinates.

$$P=-m_1gs_1-m_2g(s_1+s_2\cos\theta_1)-m_3g(s_1+s_2\cos\theta_1+s_3\cos(\theta_1+\theta_1))+(0.5)k_{11}(s_1+(l/2)\theta_1-s_{01})^2+ (0.5)k_{21}(s_1-(l/2)\theta_1-s_{01})^2+(0.5)k_{12}(s_2+(l/2)\theta_2-s_{02})^2+(0.5)k_{22}(s_2-(l/2)\theta_2-s_{02})^2+(0.5)k_{13}(s_3+ (l/2)\theta_3-s_{03})^2+(0.5)k_{23}(s_3-(l/2)\theta_3-s_{03})^2 \quad (4.5)$$

where, s_{01},s_{02} and s_{03} are the initial values of s_1,s_2 and s_3 respectively.

Due to viscous damping in the system, Rayliegh's dissipation function [55] is used to give damping energy

$$D'=(0.5)c_{11}(\dot{s}_1+(l/2)\dot{\theta}_1)^2+(0.5)c_{21}(\dot{s}_1-(l/2)\dot{\theta}_1)^2+(0.5)c_{12}(\dot{s}_2+(l/2)\dot{\theta}_2)^2+(0.5)c_{22}(\dot{s}_2-(l/2)\dot{\theta}_2)^2+ (0.5)c_{13}(\dot{s}_3+(l/2)\dot{\theta}_3)^2+(0.5)c_{23}(\dot{s}_3-(l/2)\dot{\theta}_3)^2. \quad (4.6)$$

The generalized forces in the system corresponding to the generalized co-ordinates are expressed as appropriately weighted combinations of the input forces. For details on the derivation, refer to appendix B.

$$Q_{s_1}=F_{11}+F_{21}+(F_{12}+F_{22})\cos\theta_1+(F_{13}+F_{23})\cos(\theta_1+\theta_2) \quad (4.7)$$

$$Q_{s_2} = F_{12} + F_{22} + (F_{13} + F_{23})\cos(\theta_2) \tag{4.8}$$

$$Q_{s_3} = F_{13} + F_{23} \tag{4.9}$$

$$Q_{\theta_1} = (l/2)(F_{11} - F_{21}) + (l/2)(F_{12} - F_{22}) + (l/2)(F_{13} - F_{23}) + s_2 \sin\theta_2 (F_{13} + F_{23}) \tag{4.10}$$

$$Q_{\theta_2} = (l/2)(F_{12} - F_{22}) + (l/2)(F_{13} - F_{23}) \tag{4.11}$$

$$Q_{\theta_3} = (l/2)(F_{13} - F_{23}). \tag{4.12}$$

It can be evinced from the force expressions that the total input forces acting on each module can be resolved into an additive component along the direction of extension and a subtractive component that results in a torque. For the first module, there is an additional torque produced by forces in the third module.

The model resulting from the application of Lagrange's equations of motion obtained for this system can be represented in the form

$$F_{coeff}\,\underline{\tau} = D(\underline{q})\ddot{\underline{q}} + C(\underline{q})\dot{\underline{q}} + G(\underline{q}) \tag{4.13}$$

where $\underline{\tau}$ is a vector of input forces and $\underline{q}$ is a vector of generalized co-ordinates. The force coefficient matrix F_{coeff} transforms the input forces to the generalized forces and torques in the system. The inertia matrix, D is composed of four block matrices. The block matrices that correspond to pure linear accelerations and pure angular accelerations in the system (on the top left and on the bottom right) are symmetric. The matrix C contains coefficients of the first order derivatives of the generalized co-ordinates. Since the system is nonlinear, many elements of C contain first order derivatives of the generalized co-ordinates. The remaining terms in the dynamic equations resulting from gravitational potential energies and spring energies are

collected in the matrix G. The coefficient matrices of the dynamic equations are given below,

$$\text{Fcoeff}=\begin{pmatrix} 1 & 1 & \cos(\theta_1) & \cos(\theta_1) & \cos(\theta_1+\theta_2) & \cos(\theta_1+\theta_2) \\ 0 & 0 & 1 & 1 & \cos(\theta_2) & \cos(\theta_2) \\ 0 & 0 & 0 & 0 & 1 & 1 \\ l/2 & -l/2 & l/2 & -l/2 & l/2+s_2\sin(\theta_2) & -l/2+s_2\sin(\theta_2) \\ 0 & 0 & l/2 & -l/2 & l/2 & -l/2 \\ 0 & 0 & 0 & 0 & l/2 & -l/2 \end{pmatrix},$$

$$D(\underline{q}) = \begin{pmatrix} m_1+m_2+m_3 & m_2\cos(\theta_1)+m_3\cos(\theta_1) & m_3\cos(\theta_1+\theta_2) & -m_2s_2\sin(\theta_1)-m_3s_2\sin(\theta_1)-m_3s_3\sin(\theta_1+\theta_2) & -m_3s_3\sin(\theta_1+\theta_2) & 0 \\ m_2\cos(\theta_1)+m_3\cos(\theta_1) & m_2+m_3 & m_3\cos(\theta_2) & -m_3s_3\sin(\theta_2) & -m_3s_3\sin(\theta_2) & 0 \\ m_3\cos(\theta_1+\theta_2) & m_3\cos(\theta_2) & m_3 & m_3s_2\sin(\theta_2) & 0 & 0 \\ -m_2s_2\sin(\theta_1)-m_3s_2\sin(\theta_1)-m_3s_3\sin(\theta_1+\theta_2) & -m_3s_3\sin(\theta_2) & m_3s_2\sin(\theta_2) & m_2s^2{}_2+I_1+I_2+I_3+m_3s_2^2+m_3s_3^2+2m_3s_3\cos(\theta_2)s_2 & I_2+m_3s_3^2+I_3+m_3s_3\cos(\theta_2)s_2 & I_3 \\ -m_3s_3\sin(\theta_1+\theta_2) & -m_3s_3\sin(\theta_2) & 0 & I_2+m_3s_3^2+I_3+m_3s_3\cos(\theta_2)s_2 & I_2+m_3s_3^2+I_3 & I_3 \\ 0 & 0 & 0 & I_3 & I_3 & I_3 \end{pmatrix},$$

$$
C(\underline{q}) = \begin{pmatrix}
c_{11}+c_{21} & \begin{matrix}-2m_2\sin(\theta_1)\dot{\theta}_1\\ -2m_3\sin(\theta_1)\dot{\theta}_1\end{matrix} & \begin{matrix}-2m_3\sin(\theta_1+\theta_2)\\ (\dot{\theta}_1+\dot{\theta}_2)\end{matrix} & \begin{matrix}-m_2s_2\\ \cos(\theta_1)(\dot{\theta}_1)\\ +(1/2)(c_{11}-c_{21})\\ -m_3s_2\\ \cos(\theta_1)(\dot{\theta}_1)\\ -m_3s_3\\ \cos(\theta_1+\theta_2)(\dot{\theta}_1)\end{matrix} & \begin{matrix}-2m_3s_3\\ \cos(\theta_1+\theta_2)(\dot{\theta}_1)\\ -m_3s_3\\ \cos(\theta_1+\theta_2)(\dot{\theta}_2)\end{matrix} & 0 \\
0 & c_{12}+c_{22} & \begin{matrix}-2m_3\sin(\theta_2)\\ (\dot{\theta}_1+\dot{\theta}_2)\end{matrix} & \begin{matrix}-m_2s_2(\dot{\theta}_1)\\ +(1/2)\\ (c_{12}-c_{22})\\ -m_3s_2(\dot{\theta}_1)\\ -m_3s_3\\ \cos(\theta_2)(\dot{\theta}_1)\end{matrix} & \begin{matrix}-2m_3s_3\\ \cos(\theta_2)(\dot{\theta}_1)\\ -m_3s_3\\ \cos(\theta_2)(\dot{\theta}_2)\end{matrix} & 0 \\
0 & 2m_3\sin(\theta_2)(\dot{\theta}_1) & c_{13}+c_{23} & \begin{matrix}-m_3s_2\\ \cos(\theta_2)(\dot{\theta}_1)\\ -m_3s_3(\dot{\theta}_1)\end{matrix} & \begin{matrix}-2m_3s_3(\dot{\theta}_1)\\ -m_3s_3(\dot{\theta}_2)\end{matrix} & \begin{matrix}(1/2)\\ (c_{13}-c_{23})\end{matrix} \\
(1/2)(c_{11}-c_{21}) & \begin{matrix}2m_3s_3\cos(\theta_2)(\dot{\theta}_1)\\ -2m_3s_2(\dot{\theta}_1)\\ +2m_2s_2(\dot{\theta}_1)\end{matrix} & \begin{matrix}2m_3s_3(\dot{\theta}_1+\dot{\theta}_2)\\ -2m_3s_2\cos(\theta_2)\\ (\dot{\theta}_1+\dot{\theta}_2)\end{matrix} & \begin{matrix}2m_3s_3s_2\\ \sin(\theta_2)(\dot{\theta}_2)\\ +(l^2/4)\\ (c_{11}+c_{21})\end{matrix} & \begin{matrix}m_3s_3s_2\\ \sin(\theta_2)(\dot{\theta}_2)\end{matrix} & 0 \\
0 & \begin{matrix}(1/2)(c_{12}-c_{22})+\\ 2m_3s_3\cos(\theta_2)(\dot{\theta}_1)\end{matrix} & \begin{matrix}2m_3s_3\\ (\dot{\theta}_1+\dot{\theta}_2)\end{matrix} & \begin{matrix}m_3s_3s_2\\ \sin(\theta_2)(\dot{\theta}_1)\end{matrix} & \begin{matrix}(l^2/4)\\ (c_{12}+c_{22})\end{matrix} & 0 \\
0 & 0 & (1/2)(c_{13}-c_{23}) & 0 & 0 & \begin{matrix}(l^2/4)\\ (c_{13}+c_{23})\end{matrix}
\end{pmatrix},
$$

$$G(\underline{q}) = \begin{pmatrix} -m_1 g - m_2 g + k_{11}(s_1 + (l/2)\theta_1 - s_{01}) + k_{21}(s_1 - (l/2)\theta_1 - s_{01}) - m_3 g \\ -m_2 g\cos(\theta_1) + k_{12}(s_2 + (l/2)\theta_2 - s_{02}) + k_{22}(s_2 - (l/2)\theta_2 - s_{02}) - m_3 g\cos(\theta_1) \\ -m_3 g\cos(\theta_1 + \theta_2) + k_{13}(s_3 + (l/2)\theta_3 - s_{03}) + k_{23}(s_3 - (l/2)\theta_3 - s_{03}) \\ m_2 s_2 g\sin(\theta_1) + m_3 s_3 g\sin(\theta_1 + \theta_2) + m_3 s_2 g\sin(\theta_1) + k_{11}(s_1 + (l/2)\theta_1 - s_{01})(l/2) \\ +k_{21}(s_1 - (l/2)\theta_1 - s_{01})(-l/2) \\ m_3 s_3 g\sin(\theta_1 + \theta_2) + k_{12}(s_2 + (l/2)\theta_2 - s_{02})(l/2) + k_{22}(s_2 - (l/2)\theta_2 - s_{02})(-l/2) \\ k_{13}(s_3 + (l/2)\theta_3 - s_{03})(l/2) + k_{23}(s_3 - (l/2)\theta_3 - s_{03})(-l/2) \end{pmatrix}.$$

4.4 MODEL VALIDATION

Having identified the parameters that define the shape of the continuum arm model, a simple prototype replicating the dynamics of a single section of the Octarm was built to validate the model. Two McKibben actuators of identical sizes were coupled together along their length. These actuators were assembled by enclosing a high temperature silicon rubber tubing inside a polyester mesh sleeve and one of its ends was sealed with a brass stopper and a brass connecter was fit to the other end that connects to the pressure adapter, thereby to the pressure lines. A compressor was used as a pressure source and the air flow in each of the actuator was regulated by a pressure regulator (ITV3010-01N11L4) that was controlled by an Arduino microcontroller (Arduino Duemilanove with ATMega328). The dimensions of the actuator are tabulated in Table 4.1.

The initial displacements (s_{0i}) of all three modules are taken as one-third of the unpressurized muscle length and the initial orientations (θ_{0i}) are taken as 0. Since the variation of mass with increase in air pressure is negligible, we split the value as twice the mass of an unpressurized muscle between the masses in the model. The masses of the terminal modules are made 0.06 Kg heavier than the mass of the second module since the brass connectors at either ends of the actuator constitute 60 % of the actuator weight. The value of l was taken to be twice the diameter of the sleeve.

Parameters of a single actuator	Value
Muscle length (including terminals)	0.5207 m
Muscle length (excluding terminals)	0.3937 m
Muscle diameter	0.0171 m
Mass of the actuator (unpressurized)	0.18 Kg
Variation in mass from 101.6 kPa to 344.737 kPa	1.1%
Inner and outer diameters of silicon tubing	9.5 mm, 12.7 mm
Diameter of the mesh sleeve	12.7 mm

Table 4.1: Prototype dimensions

The actuators were set to desired pressure levels by programming the Arduino board to send appropriate PWM signals to its analog outputs which were connected to the control inputs of the pressure regulators. The length of the arc was measured by running a thread along the groove formed at the centre by the coupled actuators. The orientation was measured using a

protractor. In few cases, images of the prototype were taken and orientation angles were found using image processing in MATLAB. A picture of the experimental setup is given in figure 4.4

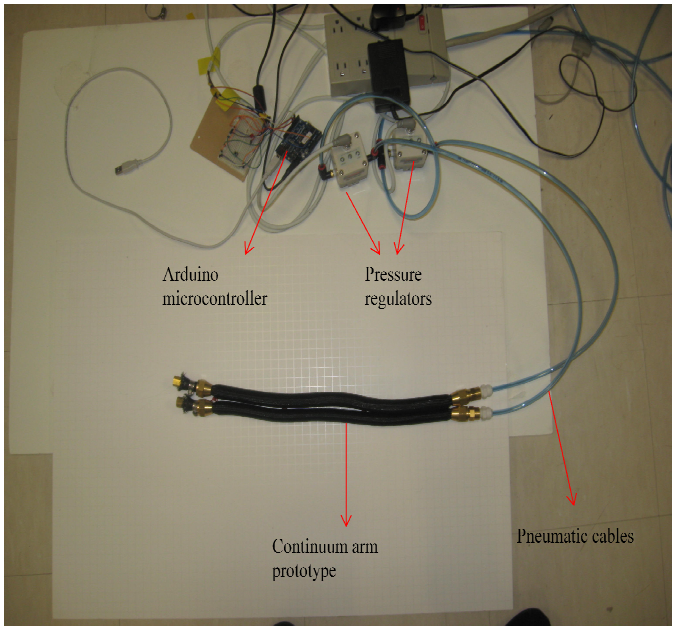

Figure 4.4: Experimental setup for taking measurements from the prototype

4.4.1 NUMERICAL RESULTS

This highly coupled nonlinear system of differential equations (equation 4.13) was solved numerically using SIMULINK™. The problem being moderately stiff, ode23t solver was chosen as the optimum solver. Also, the dynamic plots of the state variables obtained using different solvers were compared with the plot of the explicit solution of the model with equal input forces and it was confirmed that the dynamics obtained using ode23t solver matched the explicit solution.

The s_i and θ_i of all three modules in the model were summed to obtain the overall length of arc (s) and orientation (θ) of the arm model. The curvature (κ) can be evaluated using the relation between the shape parameters.

The results in table 4.1 correspond to the numerical results obtained by using the first dynamic model proposed in chapter 2 for computation of actuator forces. The actuator input force in each module is the force polynomial divided by 3. The stiffness constant of the springs in each module is three times the overall actuator stiffness. The damping coefficients are tuned so that the system is critically damped.

Actuator1 Pressure level (in kPa)	Actuator2 Pressure level (in kPa)	Measured values		Simulation results	
		s (in m)	θ (in degrees)	s (in m)	θ (in degrees)
103.421	103.421	0.405	0	0.402	0
172.362	172.362	0.435	0	0.411	0
137.894	103.421	0.425	6.66	0.406	8.67
206.841	103.421	0.430	23	0.409	17.527

Table 4.2: Measurements and numerical results with gravity in the system (actuator force as a variable of length)

Actuator1 Pressure level (in kPa)	Actuator2 Pressure level (in kPa)	Measured values		Simulation results	
		s (in m)	θ (in degrees)	s (in m)	θ (in degrees)
103.421	103.421	0.402	0	0.3968	0

172.362	172.362	0.432	0	0.408	0
137.894	103.421	0.413	52.7	0.402	27.708
206.841	103.421	0.429	84.52	0.403	58.9

Table 4.3: Measurements and numerical results without gravity in the system (actuator force as a variable of length)

The next set of tables present the results obtained by using the alternative (constant force) model for the actuators developed in the previous Chapter. The stiffness constant of the springs in each model is taken as that of the overall actuator. This is compensated by taking the actuator force in each module as the overall actuator force divided by 9 (thus having the same displacement in the model). The damping coefficients are tuned so that the system is critically damped.

Actuator1 Pressure level (in kPa)	Actuator2 Pressure level (in kPa)	Measured values		Simulation results	
		s (in m)	θ (in degrees)	s (in m)	θ (in degrees)
103.421	103.421	0.405	0	0.418	0
172.362	172.362	0.435	0	0.438	0
310.261	310.261	0.463	0	0.457	0
137.894	103.421	0.425	6.66	0.421	8.9
206.841	103.421	0.430	23	0.431	20.1
344.735	137.894	0.449	26.3	0.447	23.3
344.735	275.788	0.469	3.4	0.457	4.7

Table 4.4: Measurements and numerical results with gravity in the system (constant actuator force)

Actuator1 Pressure level (in kPa)	Actuator2 Pressure level (in kPa)	Measured values		Simulation results	
		s (in m)	θ (in degrees)	s (in m)	θ (in degrees)
103.421	103.421	0.402	0	0.401	0
172.362	172.362	0.432	0	0.426	0
310.261	310.261	0.461	0	0.451	0
137.894	103.421	0.413	52.7	0.404	41.9
206.841	103.421	0.429	84.5	0.398	118
344.735	137.894	0.445	99.9	0.385	212
344.735	275.788	0.468	27	0.447	29.7

Table 4.5: Measurements and numerical results without gravity in the system (constant actuator force)

In the case of gravity influencing the system model, it can be seen that the results produced by the constant force actuator model are better than the results produced by the length-varying actuator force function. However, for the system dynamic model without the effects of gravity, the accuracy levels of using both actuator force expressions are almost on par with each other. The inferences presented in the following paragraph are observed in both the simulation cases.

The first module had the highest displacement (followed by the second and third modules, respectively) in most of simulation cases except for several when gravitational effects were not considered in the system. These were the cases with large pressure difference in the two actuators which caused more bending and hence a decrease in displacement of module one. With gravity included in the system, the orientation angles in the terminal modules were almost the same and greater than that in the second module. However since the displacement decreased from first module to third module, the radius of curvature was almost the same in first and second modules and the third module had more curvature than the other two. This is exactly the behavior of the real device, which curls more near the tip with a nearly constant curvature throughout the rest of its structure. Without gravity in the system, the angles decreased from module one to three. This indicates a nearly constant curvature (since the displacements also decrease in the same order) throughout the length of the actuator – this phenomenon is also observed in the physical model when operated on a horizontal surface.

From the results, it can be inferred that the overall length of the arm (s) obtained from the model is very close to the values measured from the device in most cases. Our orientation measurement procedures from the physical device had a considerable error margin and hence it is unclear how precisely the model fits the device in that regard. The large difference in angles in some cases is attributed to the inability of the device to bend sufficiently to overcome the friction offered by the horizontal surface. However, since continuum robots are mostly operated in a spatial environment, we conclude that the model gives sufficiently precise information about the overall configuration of the arm. Although the analytical model can be refined by adding more

modules, a three module model appears sufficient to give a general sense of the structure of the arm as well as its configuration details.

4.4 ALTERNATIVE DYNAMICMODEL

In this section of this Chapter, a model of a Continuum arm section that was developed prior to the three module model above is described. The underlying concept of splitting a section of the arm into numerous modules was the same. However, this model incorporated the kinematics information (tip position) as well as the shape parameters in a single module. The dynamics were developed only for a single module (of a Continuum arm section). Further extension was curbed by the complexity involved in solving the highly non-linear equations associated with the model. (This restriction motivated the different modeling technique in the previous section of this Chapter.) Although this model is developed in a rudimentary form, it provides a very good insight of the forces present in the system and will be worth investigating further in the future when more effective techniques of solving are available.

Each actuator is modeled as a series of independent dynamic units, but, the position of the mass is slightly different from the other model. A rough sketch of a single module of the model is given below. The three spring-damper struts correspond to the three actuators in the (spatial) arm.

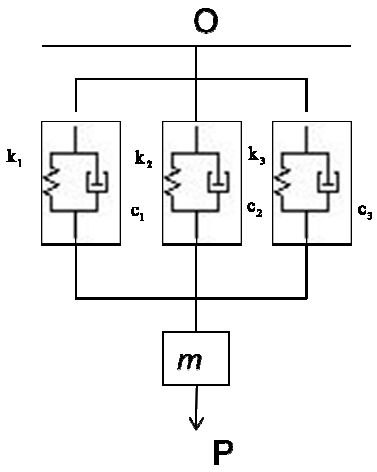

Figure 4.5: Single module of the model

The spring constants are k_1, k_2 and k_3 and the damping co-efficients are c_1, c_2 and c_3. The input actuator forces act vertically down in each of the struts. In the case of equal actuator forces, the displacement of each actuator is the same. There results in extension of the system and in this case, the model can be reduced to a simple mass, spring and damper system. The equivalent spring constants and damping coefficients for this case are given as follows.

$$k=k_1+k_2+k_3 \tag{4.14}$$

$$c=c_1+c_2+c_3. \tag{4.15}$$

The position vector and the force balance equation are given below

$$\overrightarrow{OP}=s\hat{n}_3 \tag{4.16}$$

$$F+mg-k(s-s_o)-c\dot{s}=m\ddot{s}. \tag{4.17}$$

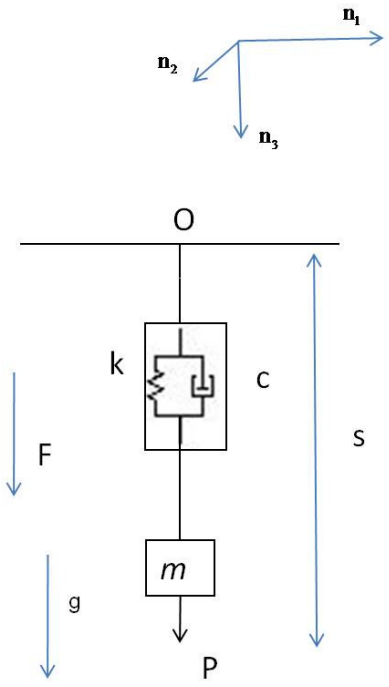

Figure 4.6: Reduced model

In the case of unequal pressures in the actuators, (i.e when arm both extends and bends) the position of the tip of the arm is given by the forward kinematics of the Octarm [18]. For making the analysis simpler, a rotating frame (B) is introduced in the model which is always oriented with the tip of the section. See Figure 4.6 below. The angle of rotation between B and N is given by θ and the corresponding rotation matrix is

$$R_N^B = \begin{bmatrix} \cos\theta & 0 & -\sin\theta \\ 0 & 1 & 0 \\ \sin\theta & 0 & \cos\theta \end{bmatrix}.$$

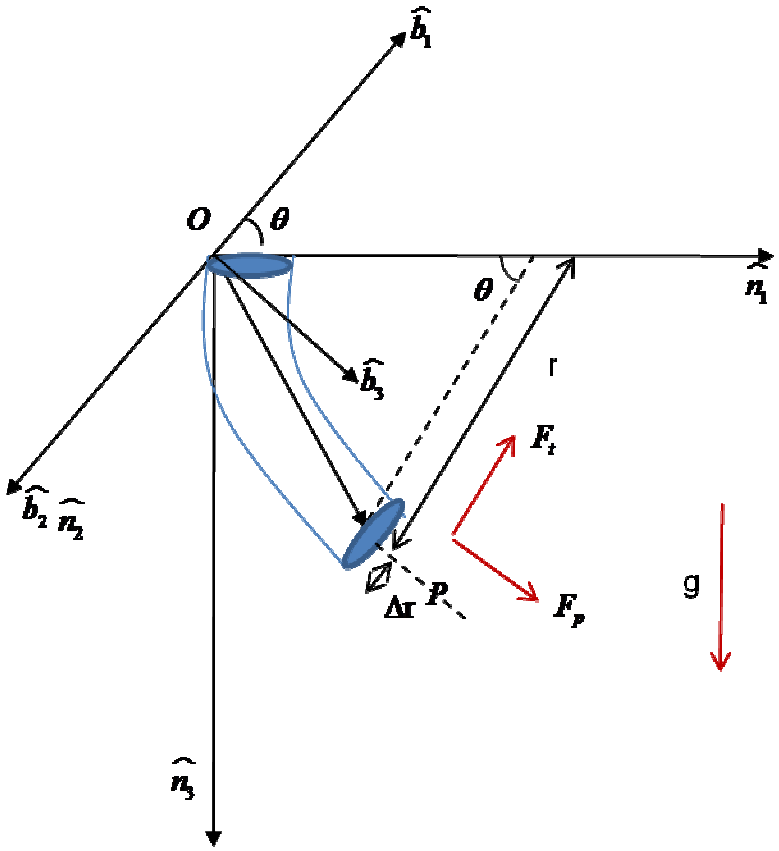

Figure 4.7: Extension and bending

The position vectors expressed with respect to both N and B frames are given below. The frame with respect to which the vector is being referred to (B or N) is indicated at the top left corner in the vector representation given below. The parameter r is the inverse of curvature (κ).

${}^{N}\overrightarrow{OP}=[r-r\cos\theta,0,r\sin\theta]$; ${}^{B}\overrightarrow{OP}=[-(r-r\cos\theta),0,r\sin\theta]$.

It is interesting to note that the position vector always bisects the angle θ. While the three module model had a force and a torque acting in each module, this model has two forces - F_p, which acts along $\hat{b}_3$ causing extension and F_t, which acts along $\hat{b}_1$ causing the model to bend.

Since the restoring forces along $\hat{b}_1$ cannot be obtained using Newtonian dynamics, we adopted a Lagrangian formulation for the derivation of the dynamic model. The kinetic energy and potential energies are given below

$$T=(0.5)m[2\dot{r}^2-2\dot{r}^2\cos\theta+r^2\dot{\theta}^2+2\dot{r}r\dot{\theta}\sin\theta], \tag{4.18}$$

$$V=-mgr\sin\theta+(1/2)[k_1((r+\Delta r)\theta-s_0)^2+k_2((r-\Delta r)\theta-s_0)^2]. \tag{4.19}$$

Raleigh's dissipation function for this model is given by

$$D'=(1/2)(c_1((r+\Delta r)\dot{\theta}+\dot{r}\theta)^2+c_2((r-\Delta r)\dot{\theta}+\dot{r}\theta)^2). \tag{4.20}$$

The generalized co-ordinates in this system are r and θ and the corresponding generalized forces are Q_r and Q_θ. Referring to Appendix B for details on derivation,

$$\begin{aligned} Q_r=&2m\dot{r}\dot{r}(1-\cos\theta)+2m\dot{r}\dot{\theta}\sin\theta+mr\ddot{\theta}\sin\theta+mr\dot{\theta}^2(\cos\theta-1)-mg\sin\theta+\\ &k_1((r+\Delta r)\theta-s_0)\theta+k_2((r-\Delta r)\theta-s_0)\theta+c_1(\theta^2\dot{r}+(r+\Delta r)\dot{\theta}\theta)+\\ &c_2(\theta^2\dot{r}+(r-\Delta r)\dot{\theta}\theta), \end{aligned} \tag{4.21}$$

$$\begin{aligned} Q_\theta=&m(r^2\ddot{\theta}+\ddot{r}r\sin\theta+2r\dot{\theta}\dot{r}-gr\cos\theta)+k_1((r+\Delta r)\theta-s_0)(r+\Delta r)+\\ &k_2((r-\Delta r)\theta-s_0)(r-\Delta r)+c_1((r+\Delta r)^2\dot{\theta}+(r+\Delta r)\dot{r}\theta)+\\ &c_2((r-\Delta r)^2\dot{\theta}+(r-\Delta r)\dot{r}\theta). \end{aligned} \tag{4.22}$$

Since the shape parameters of the Octarm (s, r, θ and κ) are coupled, it is possible to obtain the generalized forces corresponding to s and κ (Q_s and Q_κ) from Q_r and Q_θ. See Appendix B for derivation of the relationship between the forces. The generalized forces are related to the forces in the system as follows

$$Q_\theta = rF_p \tag{4.23}$$

$$Q_r = \sin\theta F_p + (\cos\theta - 1)F_t \tag{4.24}$$

$$Q_s = F_p \tag{4.25}$$

$$Q_k = r^2(\theta - \sin\theta)F_p + r^2(1 - \cos\theta)F_t \ . \tag{4.26}$$

The net extension and bending forces present in the system can be obtained from the generalized force expressions

$$F_p = Q_\theta / r \tag{4.27}$$

$$F_t = m(\ddot{r}(\cos\theta - 1) + r\dot{\theta}^2 + g\sin\theta) + k_1(s'_1 - s_0)b_1 + k_2(s'_2 - s_0)b_2 + c_1\dot{s}'_1 b_1 + c_2\dot{s}'_2 b_2 \tag{4.28}$$

where, $b_1 = \dfrac{\theta - ((r+\Delta r)/r)\sin\theta)}{\cos\theta - 1}; b_2 = \dfrac{\theta - ((r-\Delta r)/r)\sin\theta)}{\cos\theta - 1}; s'_1 = (r+\Delta r)\theta; s'_2 = (r-\Delta r)\theta.$

The next step is finding a relation between the forces in the system and the actuator input forces. It can be seen from the positioning of the mass in the module that F_p is the sum of the two actuator forces and F_t is the force resulting from the couple produced by the two unequal actuator forces.

The system coordinate values can be solved for from the dynamic equations (4.27 and 4.28) of the model.

Some interesting observations can be inferred from the generalized force expressions in this model. The generalized forces corresponding to the parameters s and θ also constitute the

restoring forces due to the springs and dampers in the model. Equation 4.23 agrees with our intuition that the variable ‘s’ and its corresponding generalized force solely represent the extension capabilities of the arm. From equation 4.25 it can be seen that the tip moves with respect to a torque at an external point. The terms constituting the pushing and the bending forces (that result from the actuator input forces) are not simple enough to enable us to initially guess and write a force balance equation. When these terms are obtained using the Lagrangian derivation, they provide more insight in understanding how unequal actuator forces split into two major components that ultimately drive the arm than by using the model in the previous section. However, since these expressions are highly coupled, it is difficult to extend this model for more than one module. As a general belief that a greater number of modules would better approximate the dynamics of a section better, it would be interesting to extend the model in this way in the future. Validation would follow subsequently.

Summarizing, as the core contribution of this chapter, we have introduced a new approach to modeling the dynamics of sections of continuum robots. The approach is based on lumped model elements (masses, springs and dampers). The model, although an approximation for a continuum structure, is seen to conveniently analyze the dynamics of the arm with selectable tradeoff in accuracy of modeling. Simulation results using the model are compared with the physical measurements of a continuum arm prototype built using McKibben actuators. The relatively simple model (compared to other techniques of modeling continuum robots) demonstrates good approximation to the physical situation. This model is a new approach to Continuum section modeling, enabling possible other novel directions to be explored further, as suggested in chapter 6.

CHAPTER FIVE

ELLIPSOID MEASURES FOR A CONTINUUM ARM SECTION

The previous chapters discussed the various necessary steps for deriving a functionally realizable dynamic model of a continuum arm section. In this chapter, we propose to use ellipsoid measures obtained from the resulting new dynamic model for analyzing the effects of external forces and impacts on a continuum arm section. This chapter basically extends the ellipsoids technique employed for rigid link robots to the realm of continuum robots. The results of the analysis and its implications are also discussed.

5.1 BACKGROUND

Ellipsoids have been previously used as measures of various kinds of performance in rigid-link robotic structures. In particular, researchers have analyzed the potential "work" or "task" space performance of robots for given robot "shapes", for various situations. This has been done via synthesis of an ellipsoid representing possible changes in variables at the tip of a manipulator corresponding to changes in the configuration (shape) variables of the manipulator. The Singular Value Decomposition (SVD) of the matrix which maps the configuration variables to the manipulator tip variables is used in forming these ellipsoids. Asada was the first to propose an ellipsoid measure - the generalized inertia ellipsoid [56] that depicts the inertial effects of a manipulator due to the nature of mass distribution along its structure. Yoshikawa proposed the manipulating and manipulating force ellipsoids for rigid link manipulators [57]. The

manipulability ellipsoids provide an insight into the possible directions that favor (or restrict) movement of the manipulator at a certain configuration. Similarly, the force ellipsoids provide information about the directions in which the tip of the manipulator can sustain or impart greater (or fewer) forces at a certain configuration. Later, Yoshikawa proposed the dynamic manipulability ellipsoid which was derived from the manipulator dynamic equation [58]. Impact ellipsoids (dynamic impact ellipsoid and generalized impact ellipsoids) developed for kinematically redundant manipulators are described in [59]. For details on Chiacchio's subsequent contributions to these types of impact ellipsoids, see [60], [61]. The theory behind developing several of the above mentioned ellipsoids is summarized in the next section of this chapter.

Gravagne and Walker developed force, manipulability and compliance ellipsoids for planar continuum manipulators [62]. Gravagne modeled the continuum arm as a parameterized curve using modal functions and the ellipsoids developed were based on this model. The work in [62] is the only work to date on ellipsoids for continuum robots. However, due to the underlying model, the approach in [62] does not lend itself to real-time computation or practical modeling of dynamic effects.

A novel contribution of this thesis, introduced in this chapter, comprises of development of new ellipsoids for measuring manipulability, force and impulse forces at the tip of a continuum arm section. To be more precise, these new ellipsoids are developed for a planar continuum arm section that is capable of extension and bending.

5.2 ELLIPSOID MEASURES

The definition and physical meaning of each of the main ellipsoids developed for robots to date are reviewed in this section. The key step in each case is to identify a linear (matrix) relationship between the variables of interest, and then to use the Singular Value Decomposition (SVD) of the associated matrix to construct the ellipsoid. The columns of the matrix U of the SVD decomposition ($U\Sigma V^T$) weighted by the singular values form the axes of the ellipsoid. For more details, see [57].

For constructing manipulability ellipsoids (probably the best-known of the robotics ellipsoid measures), the SVD of the manipulator Jacobian is computed. The Jacobian is defined by the mapping

$$\dot{\underline{x}} = J(\underline{\theta})\dot{\underline{\theta}} \tag{5.1}$$

where $\dot{\underline{x}}$ is the vector of end effector velocities, $\dot{\underline{\theta}}$ is a vector of joint velocities and $J(\underline{\theta})$ is the Jacobian of the manipulator. The (relative) magnitudes of the axes of the manipulability ellipsoid that results from the SVD of J are measures of end effector velocities in the (relative) end effector directions represented by the axes. The internal volume of the ellipsoid represents all end effector velocities that result from all possible joint velocities of unit norm or less for a given configuration. Knowing this will give a general sense of the directions in which the manipulator can comfortably move and the directions in which manipulability is relatively constrained.

The manipulating force ellipsoid is the dual of the manipulability ellipsoid and is formed from the pseudoinverse of the transpose of the Jacobian [57]. The underlying relationship of interest is

$$\underline{F}=(J(\underline{\theta})^{T})^{+}\underline{\tau} \tag{5.2}$$

where $\underline{F}$ is the vector of forces acting at the tip of the manipulator and $\underline{\tau}$ is the vector of joint torques. The axes of this ellipsoid represent the magnitude and direction of possible forces at the tip of the manipulator corresponding to unit norm changes in joint torques at a particular configuration (encoded in the Jacobian via its dependence on theta). At a particular configuration of the manipulator, the manipulating force ellipsoid represents a relative measure of forces that the manipulator can sustain or impart in different directions. This is useful in determining the configurations of a robotic arm required to impart maximum (or minimum) force in a desired direction.

Dynamic impact ellipsoids and generalized impact ellipsoids are obtained by considering the impulse force acting at the tip of the section for an infinitesimally small period of time (the time period modeling the impact of interest) in the manipulator dynamics equation. Since the joint velocities and positions remain finite in such small time periods, the Jacobian and the joint torques vanish and an expression relating impulse force and change in joint velocity is obtained. For more details on derivation, see [59]

$$\triangle\dot{\underline{\theta}} = [D(\underline{\theta})]^{-1}[J(\underline{\theta})]^{T}\hat{\underline{F}} \tag{5.3}$$

where $D(\underline{\theta})$ is the inertia matrix of the manipulator, $\hat{\underline{F}}$ is the contact impulse force and $\triangle\dot{\underline{\theta}}$ is the vector of changes in joint velocities (the dimension of this term is same as that of

acceleration). The magnitude of the axes of the dynamic manipulability ellipsoid depicts the amount of impulse force that the tip of the manipulator will experience corresponding to changes in joint velocities ($\triangle\underline{\dot{\theta}}$) that are unit norm or less. From equation (5.3), the expression for contact impulse force acting at the tip of the manipulator can be written as follows,

$$\underline{\hat{F}}=[J(\underline{\theta})^{+}]^{T}[D(\underline{\theta})]\Delta\underline{\dot{\theta}}. \tag{5.4}$$

A generalized impact ellipsoid is defined in the same way as the dynamic impact ellipsoid, but the norm of the change in joint velocities is weighted by the inertia matrix. While the dynamic impact ellipsoid can be interpreted as the contact impulse forces resulting from changes in joint velocities, the generalized impact ellipsoids are the result of changes in joint kinetic energies. The impact ellipsoids give relative measures of impulse forces that the manipulator can impart or sustain in different directions at a particular configuration. This is very useful in applications like impulsive manipulation (to hit or strike a target object) in which the impulse of a collision has to be analyzed to determine the impact (impulse) force and velocity that will be imparted to the target object. Also, if the robot arm has to sustain collisions in an operating environment, these ellipsoids tell us which configuration is ideal for the arm to sustain maximum or minimum collisions along a certain direction.

In the following, we introduce a new set of impact ellipsoids for continuum robots. The approach follows the general strategy above, but exploits the dynamic models introduced in this thesis to produce a new and computationally more efficient set of ellipsoids than previously proposed.

5.3 NEW ELLIPSOIDS: ANALYSIS AND RESULTS

The Jacobian and the inertia matrices required for plotting the new ellipsoids are obtained from the analytical model developed in Chapter 4. The inertia matrix $D(\underline{q})$ can be retrieved from the system dynamic equation (equation 4.13) in Chapter 4. To obtain the Jacobian for this model, we express the co-ordinates of the tip of the model $(x\hat{n}_1, y\hat{n}_3)$ which is same as that of the third point mass' (m_3) position vector as follows,

$$x = s_2 \sin(\theta_1) + s_3 \sin(\theta_1 + \theta_2) \tag{5.5}$$

$$y = s_1 + s_2 \cos(\theta_1) + s_3 \cos(\theta_1 + \theta_2) \tag{5.6}$$

$$\underline{\dot{x}} = J\underline{\dot{q}} \tag{5.7}$$

$$J=\begin{bmatrix} 0 & \sin(\theta_1) & \sin(\theta_1+\theta_2) & s_2\cos(\theta_1)+s_3\cos(\theta_1+\theta_2) & s_3\cos(\theta_1+\theta_2) & 0 \\ 1 & \cos(\theta_1) & \cos(\theta_1+\theta_2) & -s_2\sin(\theta_1)-s_3\sin(\theta_1+\theta_2) & -s_3\sin(\theta_1+\theta_2) & 0 \end{bmatrix}. \tag{5.8}$$

where $\bar{q}$ is a vector of generalized forces and is given by

$$\bar{q} = \begin{bmatrix} s_1 \\ s_2 \\ s_3 \\ \theta_1 \\ \theta_2 \\ \theta_3 \end{bmatrix}.$$

Thus the configuration variables of the manipulator for which the subsequent ellipses are drawn are the same as the generalized co-ordinates of the dynamic model. We have considered the physical parameters of the dynamic model to be same as that of the continuum arm prototype used for validation of the model in chapter 4. The configuration variables ($s_1, s_2, s_3, \theta_1, \theta_2$ and θ_3)

are obtained by numerically solving the model for the desired pressure levels in the two actuators. In this chapter, for drawing and analyzing the ellipsoids, we have chosen three representative configurations of a continuum arm- 1. Equal pressure levels in the actuators, in which case, the actuator extends without bending, 2. Minor difference in the pressures levels of the actuators which cause each of the actuators to extend, but, the unequal extension of the actuators imparts a curved structure to the prototype arm, 3. Significant difference between pressure levels; in this case, the configuration of the prototype arm is the same as that of case 2, but the curvature is greater.

First, the manipulability ellipsoids are drawn using the manipulator's Jacobian matrix (here, we use the dynamic model's Jacobian matrix). Figure 5.1 shows the manipulability ellipsoids drawn for three different sets of pressure levels in the air muscles of the prototype model. The difference between the two pressure levels determines the curvature of bending and the sum of the two contributes to the increase in arc length of the continuum arm. The plots corresponding to manipulator configurations of 50 psi & 50psi, 50 psi & 45 psi and 50 psi & 40 psi are shown in red green and blue respectively. A small picture depicting the shape of the manipulator and its corresponding color code is shown beside this and every subsequent plot. The directions of n_1 and n_3 axes in the figure are the same as that of the plots. The centre of each of the ellipsoids is considered to be at the centre of the tip of the manipulator.

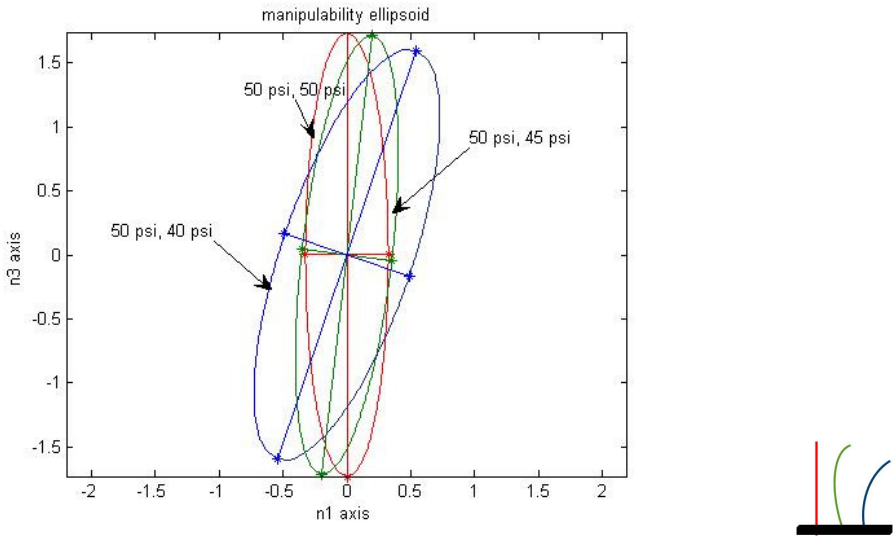

Figure 5.1: Manipulability ellipsoids

The axes of the manipulability ellipsoids represent the relative manipulator end effector (tip) velocities available in the corresponding directions for unit-norm joint velocities. The manipulability ellipsoids indicate that there is always a maximum possibility of movement along a direction which roughly approximates the direction of alignment of the continuum arm's trunk.

The manipulating force ellipsoids for three cases of actuator pressure levels are shown in figure 5.2.

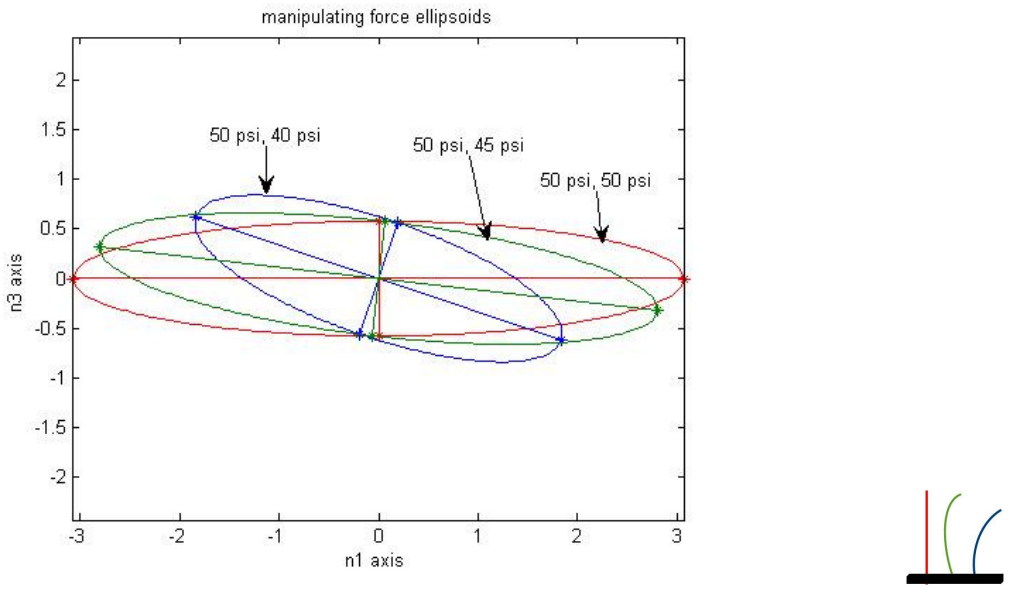

Figure 5.2: Manipulating force ellipsoids

The manipulating force ellipsoid being the dual of the manipulability ellipsoid [57] has the shape of the manipulability ellipsoid after it has been rotated by an angle of 90 degrees. The axes of the manipulating force ellipsoids represent the magnitude and direction of the forces acting at the tip of the manipulator corresponding to unit changes in shape input forces. The major and minor axes of these ellipsoids correspond to the directions that can sustain maximum and minimum forces respectively corresponding to unit change in the shape input forces. The input forces in this model will be the generalized forces. The manipulating force ellipsoid exhibits a shape such that maximum possible forces can be sustained or impacted by the arm when it sweeps its trunk across the surface where it is being laid, i.e approximately orthogonal to its direction of alignment..

The impact ellipsoids for the same three configurations are given in figure 5.3 and 5.4.

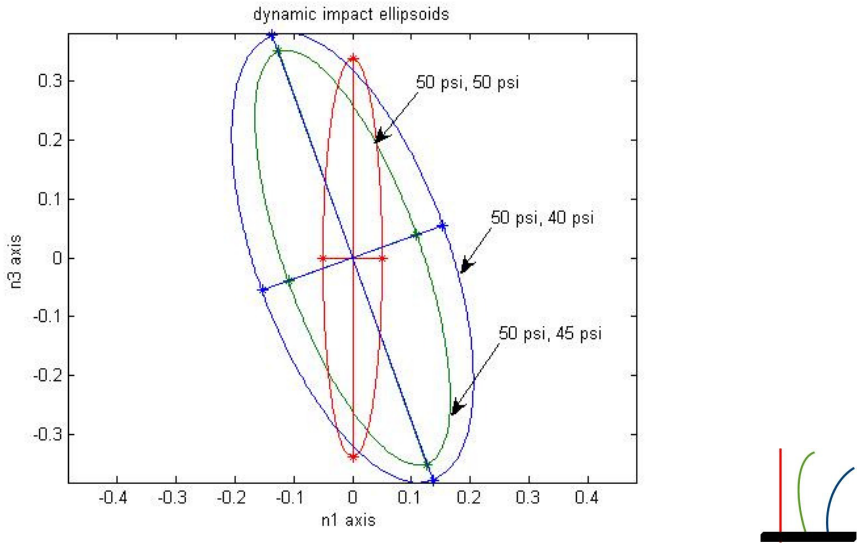

Figure 5.3: Dynamic impact ellipsoids

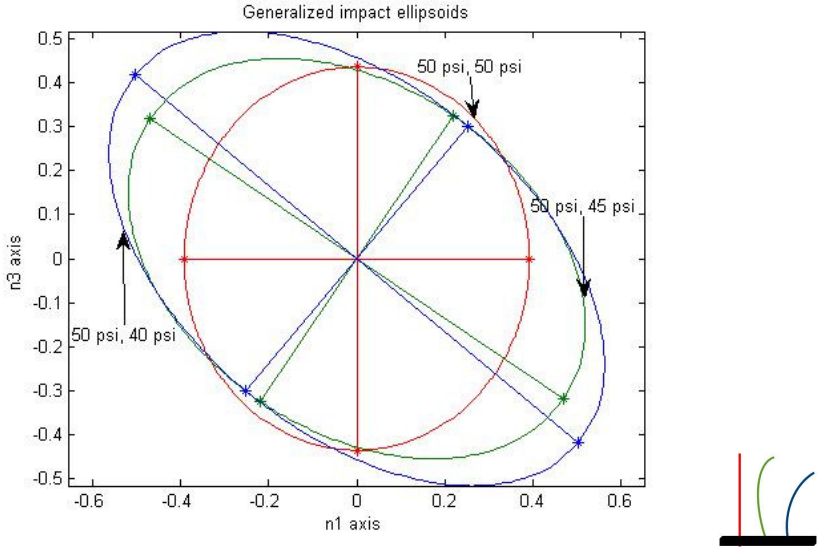

Figure 5.4: Generalized impact ellipsoids

The axes of the impact ellipsoids represent the relative magnitude and direction of the contact impulse forces acting at the tip of the manipulator. The dynamic impact ellipsoids show

the directions in which the manipulator will experience the greatest impact as well as the least impact; that is, it represents the relative magnitude of impulse forces in different directions which correspond to unit changes in joint velocities. The generalized impact ellipsoids are seen to be more isotropic when compared to the dynamic impact ellipsoids and become a perfect circle when the manipulator has zero curvature. This is because the magnitudes of the elements of the inertia matrix are nearly identical and there is a net effect of averaging out the configuration variables. Had the inertia matrix been a diagonal matrix, the configuration variables would have been weighted appropriately by the diagonal elements of the inertia matrix. These observations hold true for straight and bending (with lower curvature) configurations of the arm.

Next, the manipulability, manipulating force and impact ellipsoids are presented individually for different configurations of the continuum arm section. . From the previous set of results, one can observe the trend of variation of the orientation and shape of the ellipsoids with change in configuration of the arm. The following results concentrate on the inferences obtained from ellipsoids for specific configurations of the manipulator hardware. For each case, the prototype's configuration is shown. The red arrow in the picture of the actuator prototype indicates the orientation of the tip. This tip orientation is indicated by a black arrow in the plots.

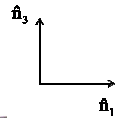
$\hat{n}_3$
$\hat{n}_1$

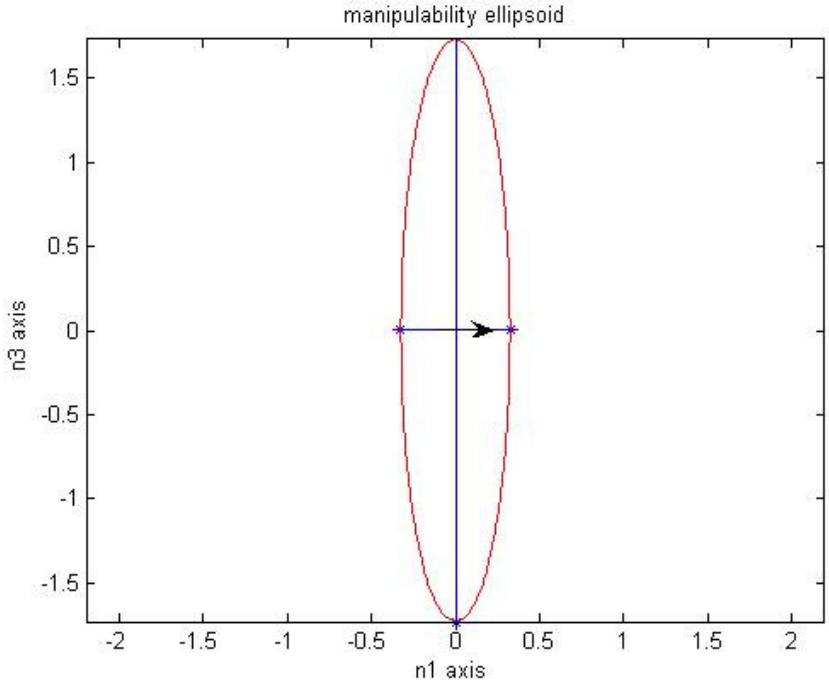
manipulability ellipsoid
n3 axis
n1 axis
1.5
1
0.5
0
-0.5
-1
-1.5
-2
-1.5
-1
-0.5
0
0.5
1
1.5
2

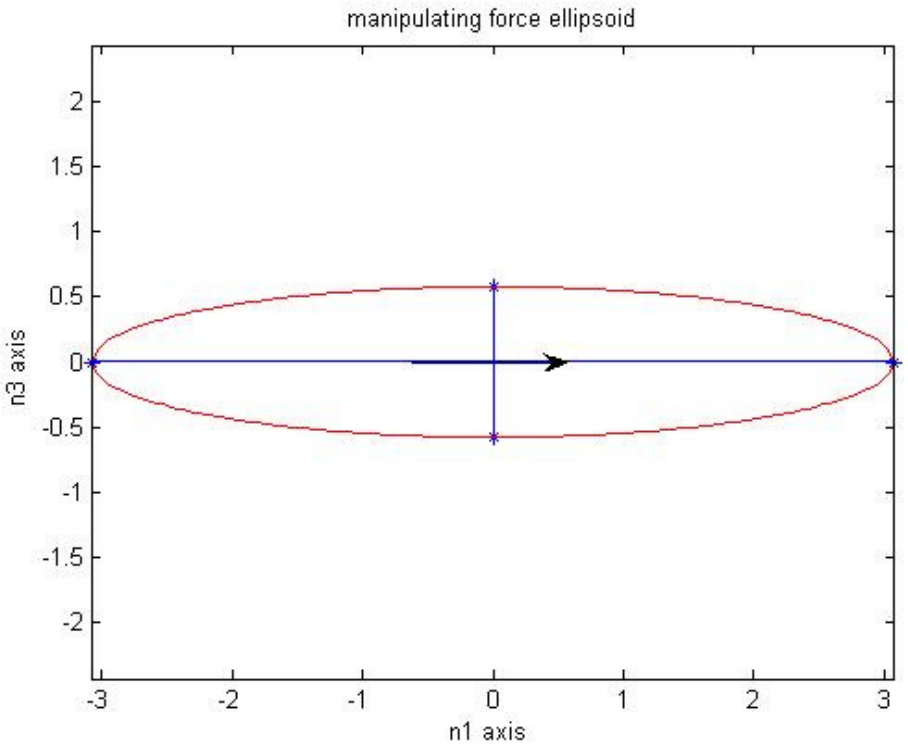
manipulating force ellipsoid
n3 axis
n1 axis
2
1.5
1
0.5
0
-0.5
-1
-1.5
-2
-3
-2
-1
0
1
2
3

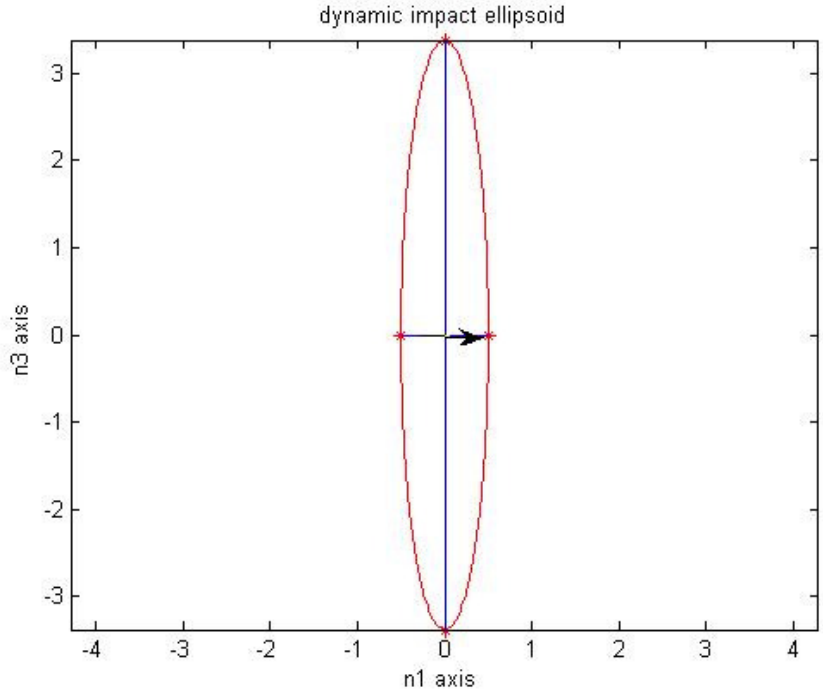
dynamic impact ellipsoid
n3 axis
n1 axis
3
2
1
0
-1
-2
-3
-4
-3
-2
-1
0
1
2
3
4

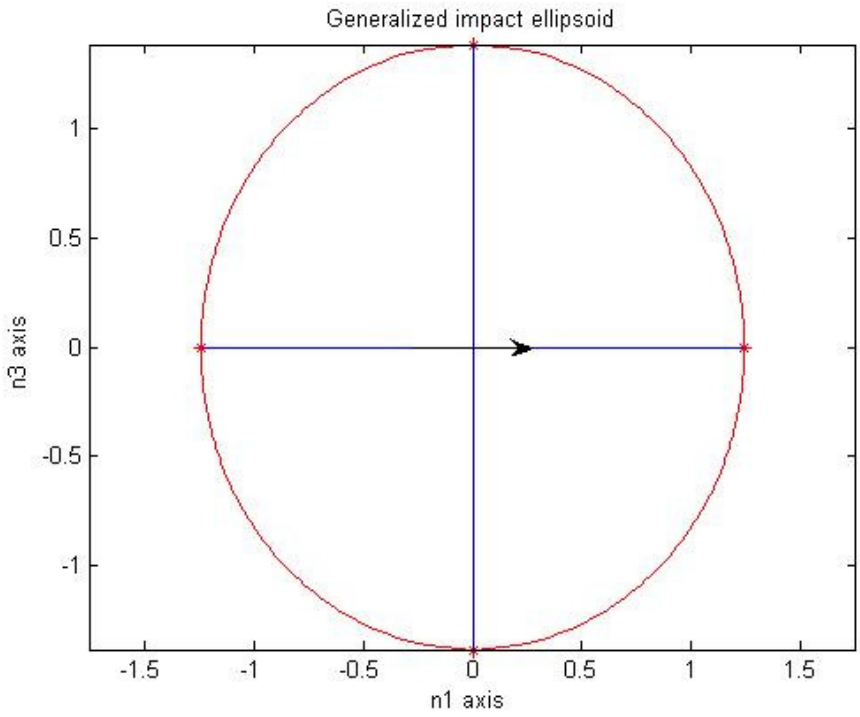

Figure 5.5: Ellipsoids drawn for equal pressures in both actuators

When there is a pressure of 50 psi in both the actuators, the manipulator extends and there is no bending. There is maximum manipulability along the length of the arm and maximum force imparted when it waves its trunk (perpendicular to its extended length). The manipulator in this configuration has the ability to withstand major impacts along the direction of the trunk. The configuration variables (obtained by numerically solving the dynamic model) for this pressure level pair are,

theta=[0 0 0]

s=[0.161 0.1511 0.1411].

The solutions (configuration variables) are represented above as arrays. Each element refers to

the corresponding variable in the first, second or third module as indicated by the index of the element. The unit of theta is in radians and that of s is in metres.

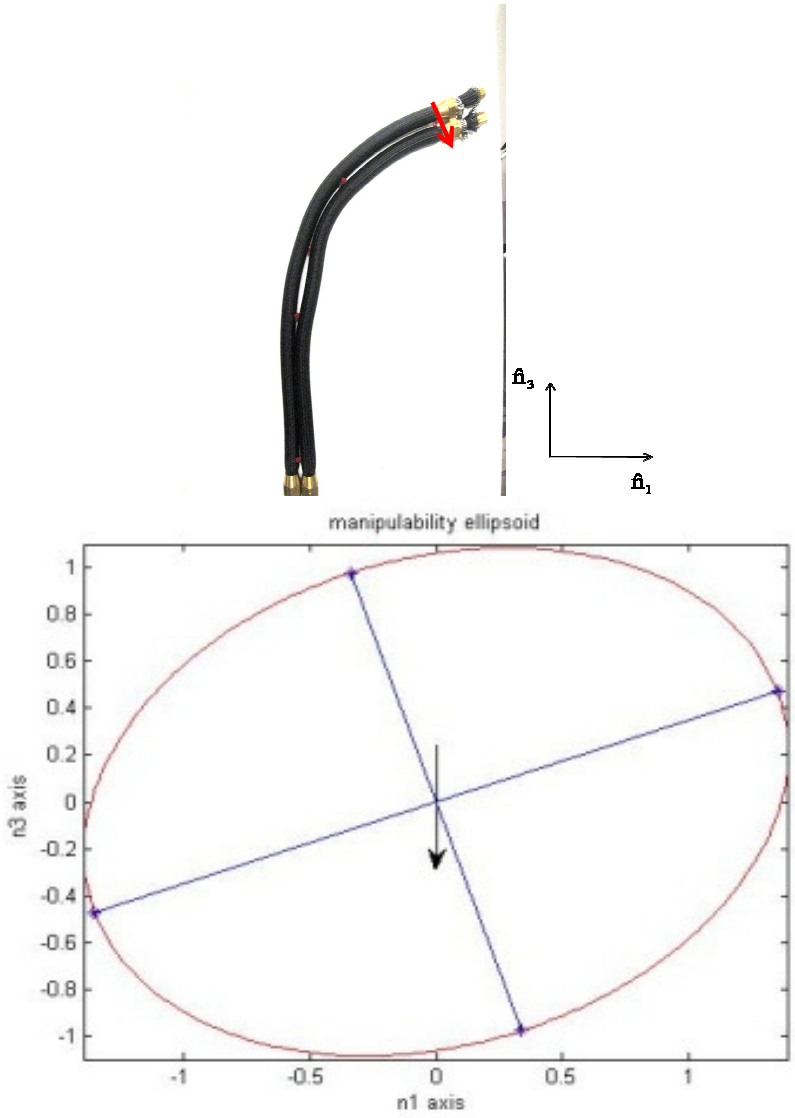

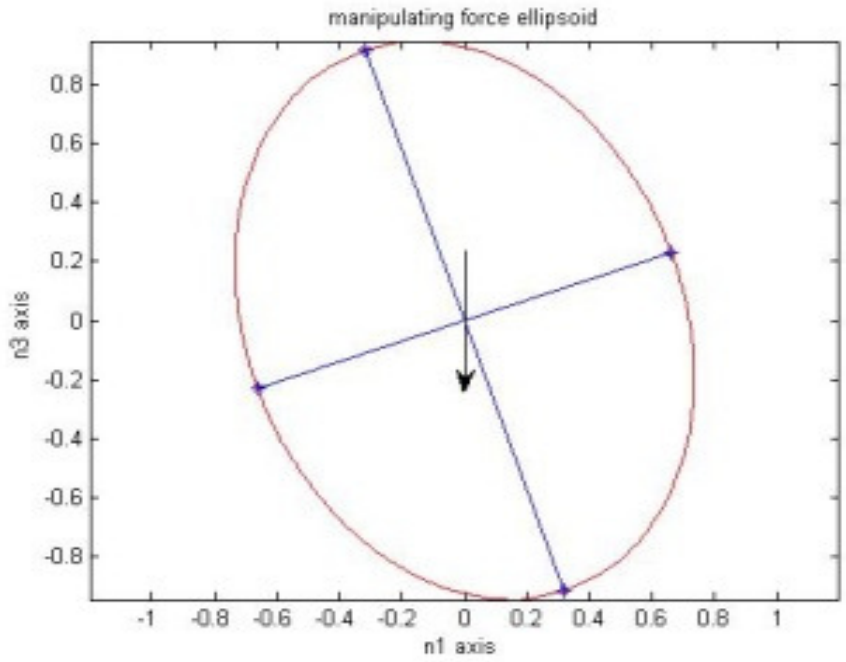
manipulating force ellipsoid
n3 axis
n1 axis
0.8
0.6
0.4
0.2
0
-0.2
-0.4
-0.6
-0.8
-1
-0.8
-0.6
-0.4
-0.2
0
0.2
0.4
0.6
0.8
1

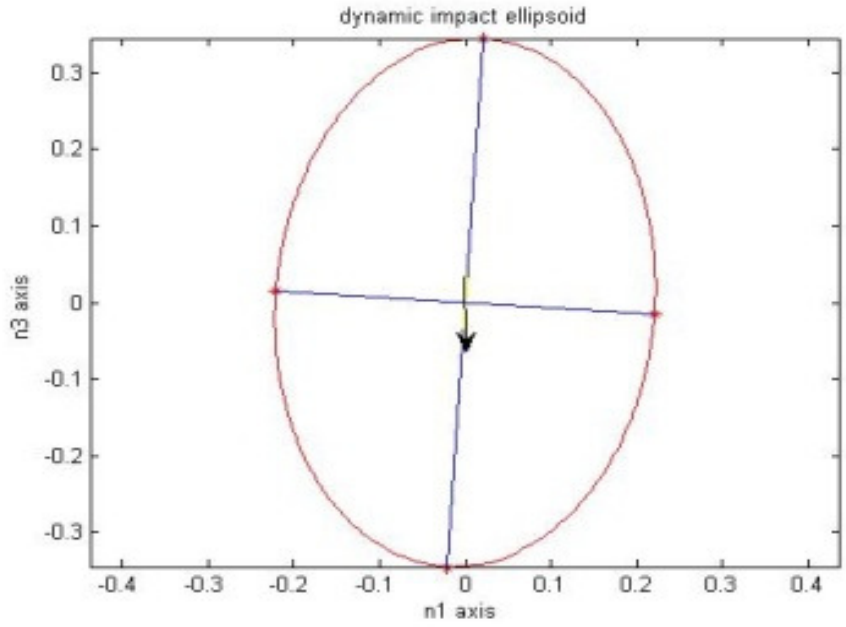
dynamic impact ellipsoid
n3 axis
n1 axis
0.3
0.2
0.1
0
-0.1
-0.2
-0.3
-0.4
-0.3
-0.2
-0.1
0
0.1
0.2
0.3
0.4

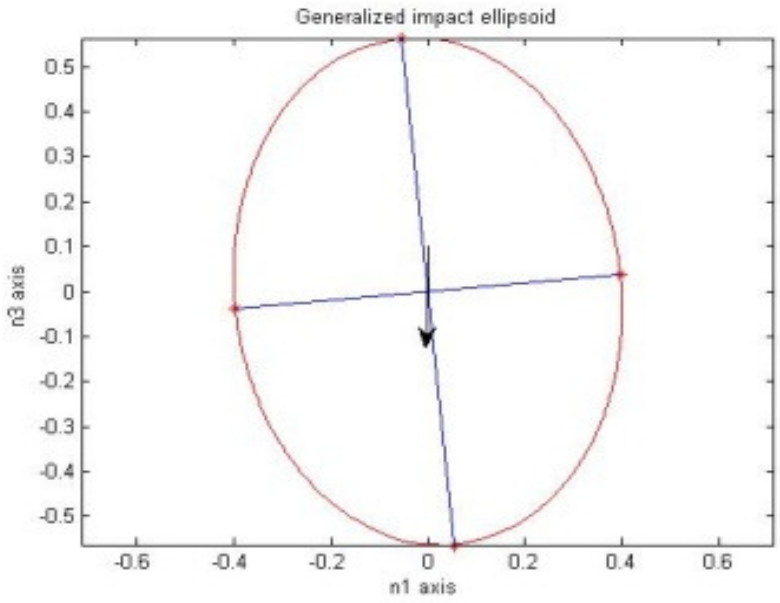

Figure 5.6: Unequal pressures in both actuators (less curvature of bending)

In this case of figure 5.6, where there is a pressure of 50 psi in one actuator and 30 psi in another, maximum manipulability is seen in a direction perpendicular to the orientation of the tip. Maximum forces act in a direction perpendicular to this and this is in line with our intuitions as how to strike an object with maximum force with the manipulator shaped in this configuration (similar to a snake executing a prey strike move to knock down a prey with maximum force) .

The configuration variables in this case are,

theta=[1.318 0.1809 0.08945]

s=[0.1376 0.1479 0.1396].

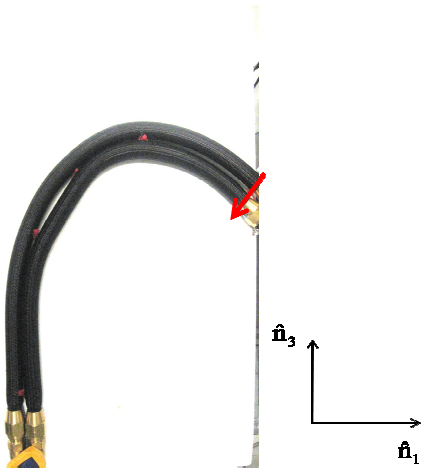
$\hat{n}_3$
$\hat{n}_1$

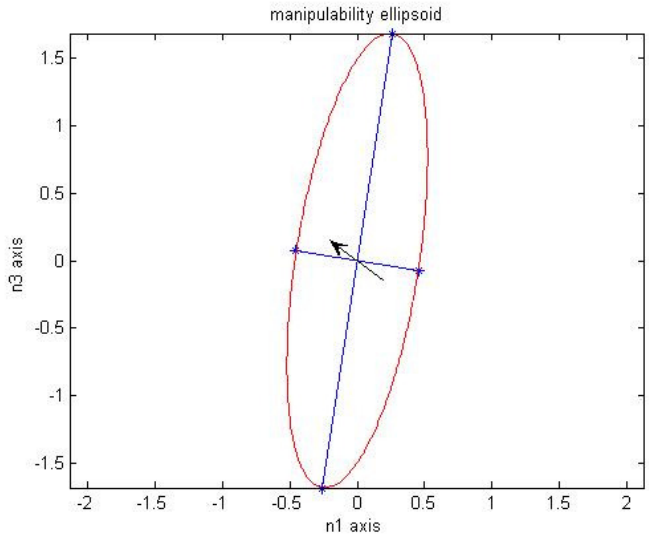
manipulability ellipsoid
n3 axis
n1 axis
1.5
1
0.5
0
-0.5
-1
-1.5
-2
-1.5
-1
-0.5
0
0.5
1
1.5
2

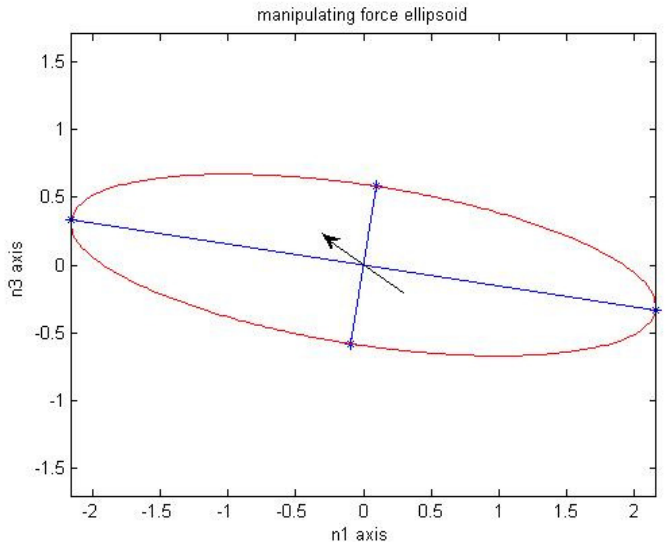
manipulating force ellipsoid
n3 axis
n1 axis
1.5
1
0.5
0
-0.5
-1
-1.5
-2
-1.5
-1
-0.5
0
0.5
1
1.5
2

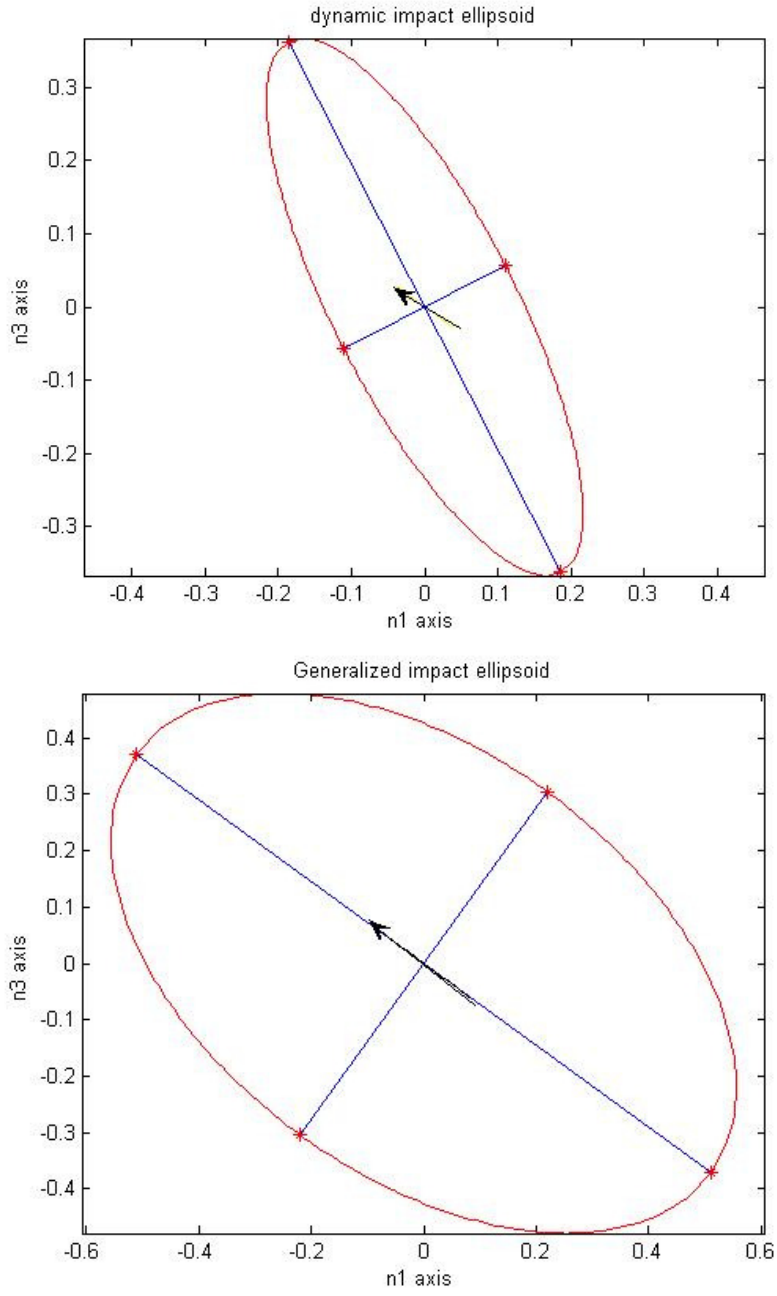

Figure 5.7: Unequal pressures in both actuators (more curvature of bending)

The above case corresponds to pressure levels of 50 psi and 20 psi. The orientations and shape of the four different types of ellipsoids follow the same explanation as that of the previous case.

The configuration variables for this case are,

theta=[3.184 0.3983 0.1909]

s=[0.1029 0.1438 0.1379].

The next set of ellipsoids depict the behavior of the manipulator when there is an impulse force acting at its tip with increase/decrease in the magnitude of the point masses in the model. The change in shape of the impact ellipsoids when all the masses in the model are scaled up/down uniformly by a factor of 10 are given in Fig. 5.8.It can be seen that the size of the ellipsoids vary but the orientation is not affected. The result is shown for the case where the extension and bending for the original mass value corresponds to the 50 psi, 40 psi case.

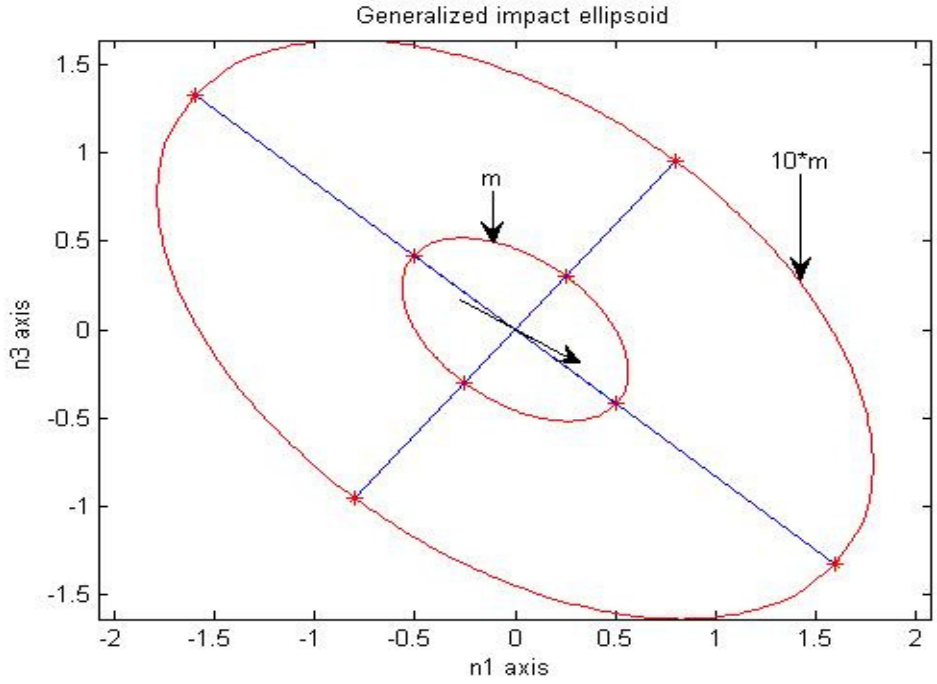

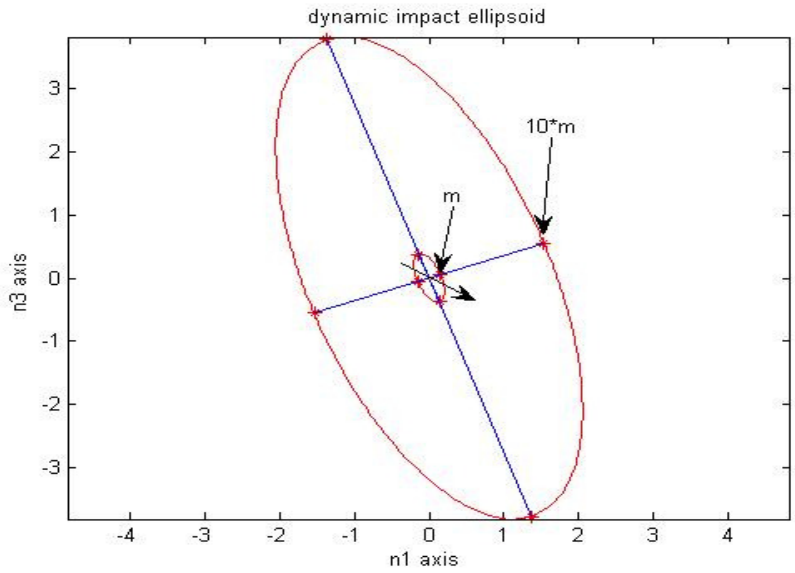

Figure 5.8: Impact ellipsoids for uniform variation of mass

In the next case, the effects of increasing the magnitude of the point mass at the tip of the manipulator (m3) by a factor of 10 are analyzed.

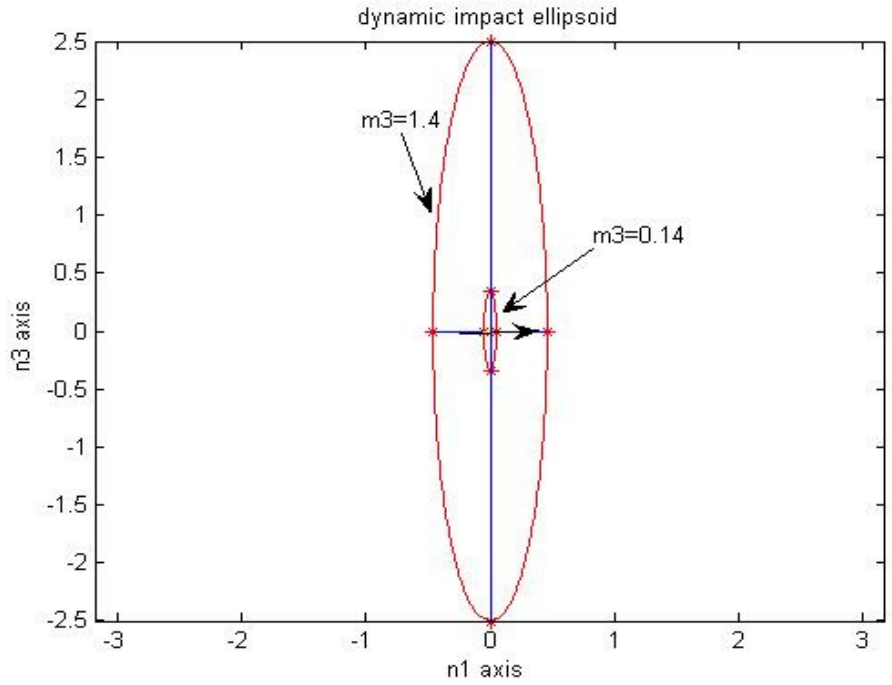
dynamic impact ellipsoid
m3=1.4
m3=0.14
n3 axis
n1 axis
2.5
2
1.5
1
0.5
0
-0.5
-1
-1.5
-2
-2.5
-3
-2
-1
0
1
2
3

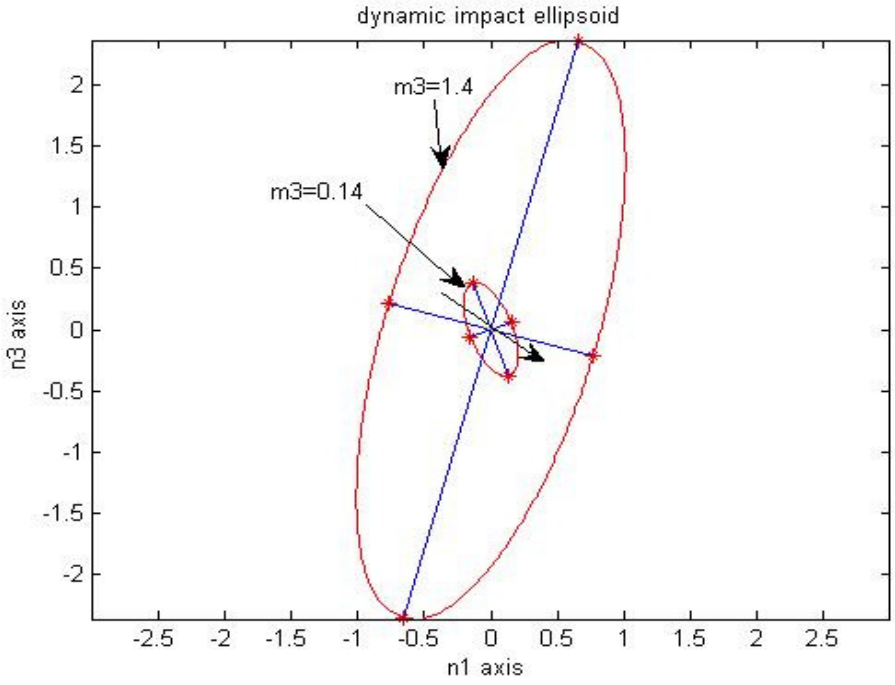
dynamic impact ellipsoid
m3=1.4
m3=0.14
n3 axis
n1 axis
2
1.5
1
0.5
0
-0.5
-1
-1.5
-2
-2.5
-2
-1.5
-1
-0.5
0
0.5
1
1.5
2
2.5

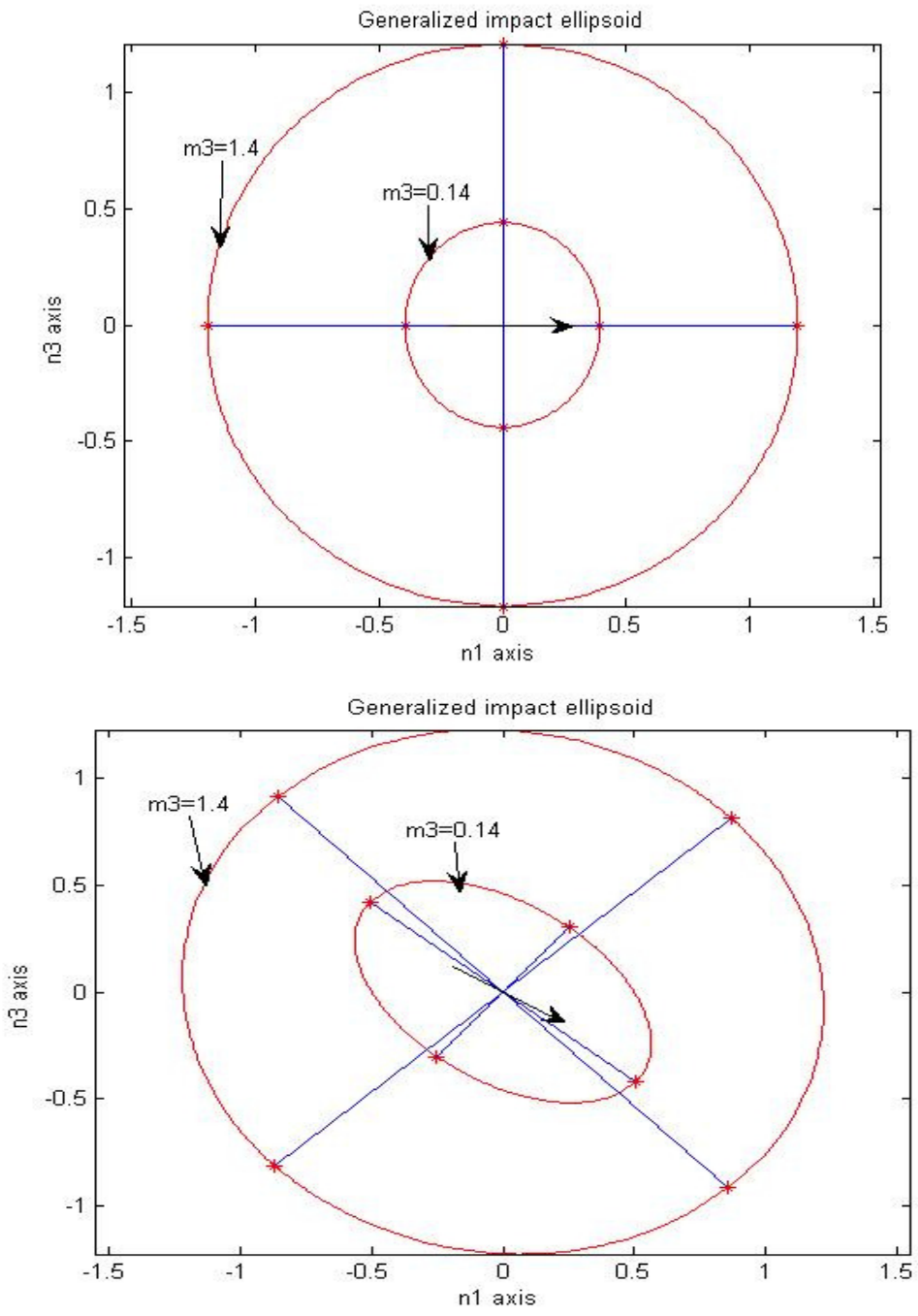

Figure 5.9: Impact ellipsoids when terminal mass is increased

The first pair of plots above corresponds to the 50 psi, 50 psi case and the second pair of plots corresponds to the 50 psi, 40 psi case. The increase in volume of the ellipsoids can be

attributed to the increase in overall mass of the arm. The change in orientation of the ellipsoids makes sense intuitively since with increase in terminal mass, there is a completely new direction in which larger impact forces produce same changes in joint velocities.

In this Chapter, ellipsoids for measuring force and velocity manipulability and also impacts for a continuum arm section prototype (using the Jacobian and inertia matrices introduced earlier in the Thesis) are developed and analyzed for different manipulator configurations. Using the linear approximation model for developing the system dynamics eliminates the need to use highly complicated Jacobian and inertia matrices for a continuum arm. The resulting ellipsoids both support existing understanding and give rise to new insight. The effects of variation of the size and orientation of the ellipsoids with change in mass distribution along the length of the arm is readily observed. The manipulability ellipsoids formed using the approximated model of the continuum arm provides new insight into the possible directions that favor movement at a configuration. Similarly, the force and the impact ellipsoids provide information about the directions in which the tip of the manipulator can sustain more force and impacts respectively. Note that the results produce insight which is quite different to those for conventional rigid-link robots. For example, in the “straight line backbone” configuration, rigid-link robots exhibit maximum manipulability (and minimum force capacity) in the direction perpendicular to the “backbone”, and maximum force capacity (and minimum manipulability) along the backbone. However, the ellipsoids herein indicate that the opposite is true for continuum sections, as discussed earlier in this chapter. Reflecting on the physical “duality” between rigid-link and continuum robots supports these results. The very rigidity of discrete

links induces high force capacity along their length, where the very compliance of continuum sections induces low force capacity along theirs. A similar duality follows for manipulability.

From the depth of information acquired from these ellipsoids, it appears that this technique will serves as a promising tool for examining the capabilities of continuum arm robot for a plethora of applications. This feature combined with the inherent usability of the linear dynamic model can be exploited for studying the interaction of the arm over various situations that are likely to be encountered in practical environments where continuum robots might be deployed and operate. More discussion on refining this work to thereby making it more effective and practical is given in Chapter 6.

CHAPTER SIX

CONCLUSIONS AND FUTURE WORK

6.1 CONCLUSIONS

The foundation of the main technical material presented in this thesis is laid in chapter 2 starting from the description of the kinematics and operation of Octarm VI continuum robot. A study on using continuum robots for real world continuum grasping applications is presented highlighting the areas of grasping that require a knowledge of the system dynamics. It is essential to develop a dynamic model to optimize the grasp points, trajectories and operational velocities of the arm in grasping. Apart from the observations made, the potential of Octarm VI in continuum grasping is quantified using measured physical data such as compliance (in the lateral direction) of the sections, curvatures of the sections, payload and speed of operation.

In chapter 3, a detailed coverage of the description and working principle of McKibben actuators that form the backbone of most of the practically built continuum robots is given. The actual force model proposed by Chou and Hannaford predicts a certain length (braid angle) at which the forces become zero. However, the measured values of forces do not follow this predicted trend. Two force models for extensors to be used in the dynamic model are proposed - one is based on Chou and Hannaford's model for contractors and the other one is a set of force expressions (for different pressure levels) as a function of actuator length. The latter model is based on the results of experimental characterization. The actuator stiffness is found to increase

linearly with pressure levels. The theoretical and experimental results presented in this chapter are significant contributions to extensor actuator dynamic modeling.

Chapter 4 presents the main results of the thesis. The steps involved in the derivation of a new analytical model of a single section of a continuum arm using lumped parameter elements are explained in detail. The results of numerical simulation are fairly close to the measurements taken from the continuum arm prototype when gravity acts on the system. The generalized co-ordinates (which are being solved for) of the three modules accurately describe the configuration of the arm for cases with and without gravity. The overall simulation results obtained by having a constant actuator force model are more accurate than having a length-varying actuator force model. The novel approach for modeling continuum robots introduced in this chapter is more suited for practical implementation than those previously appearing in the literature. The presentation also provides ideas for developing an alternative novel model based on the same underlying concept of lumped parameter modeling which can be solved with sophisticated computational techniques.

In chapter 5, new ellipsoids to measure manipulability, end effector forces and impacts have been developed based on the dynamic model for a continuum section introduced in the earlier Chapters. The shapes and orientations of the manipulability and manipulating force ellipsoids for different configurations of the continuum arm section easily match our intuitions. However, the impact ellipsoids provide us with new insights about the abilities of the continuum arm structure to sustain contact impulsive forces at its tip at different configurations. This technique aids modeling of continuum arms and also in analyzing the capabilities of such

structures (in terms of velocity and force manipulability and continuum sections capabilities to withstand impact) at different configurations.

6.2 SUGGESTIONS FOR FUTURE WORK

Ideas and suggestions for the improvement of different facets of the work presented in this thesis are enumerated in this section. The immediate next step towards enhancement of the work will be increasing the accuracy of the simulation results (with respect to matching the shape of the actual hardware) of the dynamic model. An obvious approach to this will be to increase the number of modules that are incorporated in the model. When an increased number of modules is added to the model, the precision of representation of the continuum arm structure will be increased, since, in the ideal case, a continuum arm model would be comprised of an infinite number of modules. When efficient computational techniques for solving the system dynamics are developed and available, it will become increasingly worthwhile to invest the effort to simulate the model with multiple additional modules incorporated.

Another aspect of the modeling in which a major enhancement can be effected is in the characterization of the actuator forces. As noted in the concluding lines of chapter 3, modeling an extensor is a new and vast topic by itself and the amount of research accomplished at present is still in its initial stages. The complex interactions between various forces originating from the movement of braids and tubing (that are dependent on the material properties and structure of the braids and tube respectively) are yet to be fully explained and modeled. If there is a substantial progression in this direction resulting in the development of a better model that more closely

matches the measured forces at various lengths and pressures, it will represent a significant step in dynamic modeling. Also, when more than one muscle is coupled to form a planar or a spatial continuum arm there is a considerable interaction between the interaction forces exerted by the different actuators, which calls for additional force models to be incorporated in the dynamic model.

In the context of the ellipsoid measures, there is ample scope to extend the technique introduced in this Thesis to continuum arm models with more than one section, with or without extending the dynamic model to higher numbers of modules. Having observed a pattern in the elements of the inertia and the Jacobian matrices of the three module model, it is possible to form the inertia matrix and Jacobian for a two section continuum arm model (this can be envisioned as having two single section models connected in series). Theoretically, it is possible to extend the inertia and Jacobian matrices for any number of sections; however the expanded inertia matrix quickly becomes complicated. Thus, extension of this technique for more than two sections may not be the most fertile area for research at this stage.

With all the suggestions stated above taken into consideration, the dynamic model and the new set of ellipsoids developed in this Thesis should serve as effective tools for studying a continuum robot's response to influential forces and impacts that will be encountered in an operating environment. This matches the larger goal of realizing practical models of continuum robots that will aid in deploying these robots in a diversified range of practical applications.

APPENDIX

Appendix A: Actuator Parameters

The notes in this Appendix explain how the various critical actuator parameters in Chapter 3 were calculated.

Diameter of the unpressurized actuator (D): 17.1 mm (measured using calipers).
Length of the unpressurized actuator (L): 0.4 m.

According to the method described in [63] to calculate the actuator parameters, the term, B is defined as the number of trapezoids formed by the braids along the circumference of a sleeve. According to [63], D is given by

$D = \frac{2Bl\sin\psi}{\pi}$, where l is the length of a side of the trapezoid which was measured to be 1.25mm.

This yielded an initial braid angle (ψ) of (63.5^{o}) for B=24. From the triangle formed by a single thread in the braid,

$L=b\cos\psi$.

The value of b was found to be 0.8965 m. Also,

$n = \frac{b\sin\psi}{\pi D}$.

The value of n approximated to the nearest integer was 15.

Appendix B: Dynamic Modeling

The intermediate steps and calculations involved in the derivation of the dynamic models described in chapter 4 are detailed in this appendix.

Firstly, the position vector of each of the masses in the primary model (three module lumped element model) described in chapter 4 is given below. Refer to figure 4.3 for the location of the three point masses within the model. The position vectors of each of the point masses referenced with respect to its corresponding local frames are,

$${}^{l_i}P_{m_i} = s_i \hat{n}_3 \qquad i=1,2 \text{ and } 3.$$

Recollect that the local frame of each module is located at the origin of the corresponding module and oriented along the variable 's' of the module. The base frame of the model is located at the origin of the first module. The rotation matrices between the local frames (l_1,l_2 and l_3) and the base frame (N) of the model are given below,

$$R_{l_1}{}^{N} = \begin{pmatrix} 1 & 0 & 0 \\ 0 & 1 & 0 \\ 0 & 0 & 1 \end{pmatrix}; \; R_{l_2}{}^{N} = \begin{pmatrix} \cos(\theta_1) & 0 & \sin(\theta_1) \\ 0 & 1 & 0 \\ -\sin(\theta_1) & 0 & \cos(\theta_1) \end{pmatrix}$$

$$R_{l_3}{}^{N} = \begin{pmatrix} \cos(\theta_1+\theta_2) & 0 & \sin(\theta_1+\theta_2) \\ 0 & 1 & 0 \\ -\sin(\theta_1+\theta_2) & 0 & \cos(\theta_1+\theta_2) \end{pmatrix}.$$

The translations between the frame origins are given as follows,

$$T_{l_1}^{\ N}=\begin{pmatrix}0\\0\\0\end{pmatrix};\ T_{l_2}^{\ N}=\begin{pmatrix}0\\0\\s_1\end{pmatrix};\ T_{l_3}^{\ N}=\begin{pmatrix}s_2\sin\theta_1\\0\\s_1+s_2\cos\theta_1\end{pmatrix}.$$

The position vectors given in chapter 4 (equations 4.1, 4.2 and 4.3) are obtained by applying the appropriate rotations and translations to the locally referenced position vectors (stated initially in this Appendix).

The Lagrangian (L) is the difference between the kinetic energy and the potential energy terms,

L=T-P.

A general expression for generalized forces, Q_k in terms of applied forces, F_j for a system having 'p' number of forces and 'n' number of generalized co-ordinates is given as follows [64],

$$Q_k=\sum_{j=1}^{p}F_j.\frac{\partial \dot{r}_j}{\partial \dot{q}_k},\qquad k=1,2,...,n.$$

The points at which the actuator forces act (r_j) are referenced initially in their respective local frames and then rotated and translated to be referenced in the base inertial frame. The points (referenced with respect to the base inertial frame) at which the forces act are given below,

F_{11} acts at $(s_1+(l/2)\theta_1)\hat{n}_3+(-l/2)\hat{n}_1$

F_{21} acts at $(s_1-(l/2)\theta_1)\hat{n}_3+(l/2)\hat{n}_1$

F_{12} acts at $(s_1+(l/2)\sin(\theta_1)+(s_2+(l/2)(\theta_2))\cos(\theta_1)))\hat{n}_3+((-l/2)\cos(\theta_1)+(s_2+(l/2)(\theta_2))\sin(\theta_1))\hat{n}_1$

F_{22} acts at $(s_1-(l/2)\sin(\theta_1)+(s_2-(l/2)(\theta_2))\cos(\theta_1)))\hat{n}_3+((l/2)\cos(\theta_1)+(s_2-(l/2)(\theta_2))\sin(\theta_1))\hat{n}_1$

F_{13} acts at $(s_1+s_2\cos(\theta_1)+(l/2)\sin(\theta_1+\theta_2)+(s_3+(l/2)(\theta_3))\cos(\theta_1+\theta_2)))\hat{n}_3+$
$((-l/2)\cos(\theta_1+\theta_2)+(s_3+(l/2)(\theta_3))\sin(\theta_1+\theta_2)+s_2\sin(\theta_1))\hat{n}_1$

F_{23} acts at $(s_1+s_2\cos(\theta_1)-(l/2)\sin(\theta_1+\theta_2)+(s_3-(l/2)(\theta_3))\cos(\theta_1+\theta_2)))\hat{n}_3+$
$((l/2)\cos(\theta_1+\theta_2)+(s_3-(l/2)(\theta_3))\sin(\theta_1+\theta_2)+s_2\sin(\theta_1))\hat{n}_1$.

Similarly, the actuator forces expressed with respect to the base frame are given below,

$$F_{11}=F_{11}\hat{n}_3$$

$$F_{21}=F_{21}\hat{n}_3$$

$$F_{12}=F_{12}\cos(\theta_1)\hat{n}_3+F_{12}\sin(\theta_1)\hat{n}_1$$

$$F_{22}=F_{22}\cos(\theta_1)\hat{n}_3+F_{22}\sin(\theta_1)\hat{n}_1$$

$$F_{13}=F_{13}\cos(\theta_1+\theta_2)\hat{n}_3+F_{13}\sin(\theta_1+\theta_2)\hat{n}_1$$

$$F_{23}=F_{23}\cos(\theta_1+\theta_2)\hat{n}_3+F_{23}\sin(\theta_1+\theta_2)\hat{n}_1.$$

The s and θ dynamic equations are as follows.

$$\frac{\partial}{\partial t}\left(\frac{\partial L}{\partial \dot{s}_i}\right)-\frac{\partial L}{\partial s_i}+\frac{\partial D'}{\partial \dot{s}_i}=Q_{s_i} \qquad i=1,2 \text{ and } 3.$$

$$\frac{\partial}{\partial t}\left(\frac{\partial L}{\partial \dot{\theta}_i}\right)-\frac{\partial L}{\partial \theta_i}+\frac{\partial D'}{\partial \dot{\theta}_i}=Q_{\theta_i} \qquad \text{i=1,2 and 3.}$$

As far as the second dynamic model presented in chapter 4 is concerned (section 4.4), this Appendix covers the fundamental dynamic equations and the derivation of a conversion procedure between the various generalized forces in the system. See figure 4.6 for an illustration of model and its system variables. The Lagrangian dynamic equations for the system variables in the second model are given as follows,

$$\frac{d}{dt}\left(\frac{\partial L}{\partial \dot{r}}\right)-\frac{\partial L}{\partial r}+\frac{\partial D'}{\partial \dot{r}}=Q_r,$$

$$\frac{d}{dt}\left(\frac{\partial L}{\partial \dot{\theta}}\right)-\frac{\partial L}{\partial \theta}+\frac{\partial D'}{\partial \dot{\theta}}=Q_\theta.$$

The relationship between generalized forces Q_r, Q_θ and Q_s, Q_κ can be derived as follows. It emanates from the relationship between the shape variables.

$s = r\theta$ and $\kappa = 1/r$.

The first derivatives of the two sets of system variables can be related as follows,

$$\begin{pmatrix}\dot{s}\\ \dot{\kappa}\end{pmatrix}=J\begin{pmatrix}\dot{r}\\ \dot{\theta}\end{pmatrix}$$

$$J=\begin{pmatrix}\theta & r\\ -1/r^2 & 0\end{pmatrix}.$$

Similarly the generalized forces corresponding to these system variables can be related as follows.

$$\begin{pmatrix} Q_s \\ Q_\kappa \end{pmatrix} = J^{-T} \begin{pmatrix} Q_r \\ Q_\theta \end{pmatrix}$$

$$J^{-T} = \begin{pmatrix} 0 & 1/r \\ -r^2 & r\theta \end{pmatrix}.$$

REFERENCES

[1] G. Robinson, and J. Davies, "Continuum robots – a state of the art,"*Proc. IEEE International Conference on Robotics and Automation*, Detroit, MI, 1999, vol. 4, pp. 2849-2854.

[2] V.C. Anderson and R.C. Horn, "Tensor Arm Manipulator Design", *Transactions of the ASME*, vol. 67-DE-57, pp. 1–12, 1967.

[3] S. Hirose, *Biologically Inspired Robots,* Oxford University Press, 1993.

[4] I.D. Walker, D. Dawson, T. Flash, F. Grasso, R. Hanlon, B. Hochner, W.M. Kier, C. Pagano, C.D. Rahn, Q. Zhang, "Continuum Robot Arms Inspired by Cephalopods, *Proceedings SPIE Conference on Unmanned Ground Vehicle Technology* VII, Orlando, FL, pp 303-314, 2005.

[5] R. Cieslak and A. Morecki, "Elephant Trunk Type Elastic Manipulator – a Tool for Bulk and Liquid Type Materials Transportation, *Robotica*, 17, pp. 11-16, 1999.

[6] M.W. Hannan and I.D. Walker, "Kinematics and the Implementation of an Elephant's Trunk Manipulator and other Continuum Style Robots", *Journal of Robotic Systems*, 20(2), pp. 45-63, 2003.

[7] H. Tsukagoshi, A. Kitagawa, and M. Segawa, "Active hose: an artificial elephant's nose with maneuverability for rescue operation," *Proc. IEEE International Conference on Robotics and Automation*, 2003, vol. 3, pp. 2454-2459.

[8] K. Salisbury, W. Townsend, B. Ebrman, and D. DiPietro, “Preliminary Design of a Whole-Arm Manipulation System (WAMS)”, *Proceedings IEEE International. Conference on Robotics and Automation*, pp. 254-260, 1988.

[9] K. Suzumori, S. Iikura, and H. Tanaka, “Development of Flexible Microactuator and it’s Applications to Robotic Mechanisms”, *Proceedings IEEE International Conference on Robotics and Automation*, Sacramento, California, pp. 1622-1627, 1991.

[10] K. Suzumori, S. Iikura, H. Tanaka, “Applying a flexible micro-actuator to robotics mechanics,” *IEEE Control Syst. Mag.,* vol.12, pp. 21-26, Feb. 1992.

[11] D.M. Lane, J.B.C. Davies, G. Robinson, D.J. O'Brien, J. Sneddon, E. Seaton, and E. Elfstrom, “The AMADEUS Dextrous Subsea Hand: Design, Modeling, and Sensor Processing, *IEEE Journal of Oceanic Engineering*, vol. 24, no. 1, pp. 96-111, 1999.

[12] D. Trivedi, C.D. Rahn, W.M. Kier, and I.D. Walker, “Soft Robotics: Biological Inspiration, State of the Art, and Future Research”, *Applied Bionics and Biomechanics*, 5(2), pp. 99-117, 2008.

[13] G..S. Chrikjian, “Theory and Applications of Hyperredundant Robotic Mechanisms”, Ph.D. Thesis, Department of Applied Mechanics, California Institute of Technology, 1992.

[14] G. S. Chirikjian, and J. W. Burdick, “A modal approach to hyper-redundant manipulator kinematics,” *IEEE Transactions on Robotics and Automation*, vol. 10, No. 3, Jun 1994, pp. 343354.

[15] H. Mochiyama, E. Shimemura, and H. Kobayashi, "Direct kinematics of manipulators with hyper degrees of freedom and serret-frenet formula," *IEEE International Conference on Robotics and Automation*, pp. 1653-1658, 1988.

[16] I. Gravagne, and I. D. Walker, "Kinematic transformations for remotely-actuated planar continuum robots," *IEEE International Conference on Robotics and Automation*, pp. 19-26, 2000.

[17] I. Gravagne, and I. D. Walker, "Kinematics for constrained continuum robot using wavelet decomposition," *Proceedings of the 4th Int. Conf. and Expo./Demo. on Robotics for Challenging Situations and Environments*, pp. 292-298, 2000.

[18] B. A. Jones, and I. D. Walker, "Kinematics for multi-section continuum robots," *IEEE T. Robot*., 22, 1, 43–55, 2006.

[19] M. T. Mason, W. H. Huang, and E. P. Krotkov," Impulsive Manipulation," *Proceedings of 1995 IEEE International Conference on Robotics and Automation*, vol 1, pp. 120-125 (1995).

[20] M. T. Mason, "Mechanics and Planning of Manipulator Pushing operations," *The International Journal of Robotics Research,* vol. 5, no. 3, pp. 53-71, 1986.

[21] M. W. Spong, S. Hutchison, M. Vidyasagar*, Robot Modeling and Control*, Wiley, John & Sons, Incorporated.

[22] I. Kato and K. Sadamoto, "Mechanical Hands Illustrated," *Survey Japan*, 1977.

[23] A. Bicchi, "Hands For Dexterous Manipulation and Robust Grasping: A Difficult Road Towards Simplicity", *IEEE Transactions on Robotics and Automation*, 16(6), pp 652-662, 2000.

[24] www.barrett.com

[25] www.anirudh.net/courses/emch520/html/

[26] B. Bernstein, D.A. Hall, and H.M. Trent, "On the Dynamics of a Bull Whip*", Journal of the Acoustical Society of America*, 30(12), pp. 1112-1115, 1958.

[27] J.M. Robson, "The Physics of Flycasting", *American Journal of Physics*, 58(3), pp. 234-240, 1990.

[28] B. Donald, L. Gariepy, and D. Rus, "Distributed Manipulation of Multiple Objects using Ropes", *Proceedings IEEE International Conference on Robotics and Automation*, pp. 450-457, 2000.

[29] W. McMahan, M. Pritts, V. Chitrakaran, D. Dienno, M. Grissom, B. Jones, M. Csencsits, C.D. Rahn, D. Dawson, and I.D. Walker, "Field Trials and Testing of "OCTARM" Continuum Robots", *Proc. IEEE International Conference on Robotics and Automation*, pp. 2336-2341, 2006.

[30] M. Csencsits, B.A. Jones, W. McMahan, V. Iyengar, and I.D. Walker, "User Interfaces for Continuum Robot Arms", *Proc. IEEE/RSJ International Conference on Intelligent Robots and Systems (IROS*), Edmonton, Canada, August 2005, pp. 3011-3018.

[31] B. Jones and I.D. Walker, "Practical Kinematics for Real-Time Implementation of Continuum Robots", *IEEE Transactions on Robotics*, Vol. 22, No. 6, December 2006, pp 1087-1099.

[32] W. McMahan, I.D. Walker, "Octopus-Inspired Grasp Synergies for Continuum Manipulators", *Proc. IEEE International Conference on Robotics and Biomimetics*, pp. 945-950, 2009.

[33] C. Chou, and B. Hannaford, "Measurement and modeling of McKibben pneumatic actuators," *IEEE Tans on robotics and automation*, vol. 12, issue 1, pp 90-102, 1996.

[34] C. Chou, and B. Hannaford,"Static and dynamic characteristics of McKibben pneumatic artificial muscles," *IEEE International conference on robotics and automation*, May 1994, vol.1, pp 281-286

[35] G. K. Klute, and B. Hannaford, "Accounting for elastic energy storage in McKibben artificial muscle actuators," *Transactions of the ASME*, vol. 122, pp. 386-388, June 2000.

[36] C.S. Kothera, M. Jangid, J. Sirohi, and N.M Wereley, " Experimental characterization and static modeling of McKibben actuators," *Journal of Mechanical Design*, vol. 131, issue 9, pp. 357 - 367.

[37] I. B. Denkena, "New compliant McKibben actuator driven by pneumatic actuators as a hexapod platform in robotic applications".

[38] F. Daerdin, and D. Lefeber," Pneumatic artificial muscles: actuators for robotics and automation," *European Journal of Mechanical and Environmental Engineering*, 2000.

[39] B. Tondu, and P. Lopez," Modeling and control of McKibben artificial muscle robot actuators," *IEEE Control Systems magazine*, April 2000.

[40] K. Takashima, J. Rossiter, and T. Mukai," McKibben artificial muscles using shape-memory polymer," *Sensors and Actuators A: Physical*, vol. 164, issue 1-2, pp. 116–124,2010.

[41] N. Delson, T. Hanak, K. Loewke and D. N. Miller, "Modeling and Implementation of McKibben actuators for a hopping robot," *ICAR Proc*, July 2005, pp 833- 840.

[42] R. Q. van der Linde," Design, Analysis and Control of a Low Power Joint for Walking Robots, by Phasic Activation of Mcibben Muscles," *IEEE transactions on robotics and Automation,* vol 15, no. 15,pp 499-604, august 1999.

[43] S.A. Wainwright, W.D. Biggs, J.D. Currey, and J.M. Gosline, "Mechanical Design in Organisms," *Princeton University Press*, 1976. (Chapter 7, page 295.)

[44] G. S. Chirikjian, "Hyper-Redundant manipulator dynamics: a continuum approximation," *Adv. Robot*., Vol. 9, No. 3, Jun. 1995, pp. 217243.

[45] W. Khalil, G. Gallot, O. Ibrahim and F. Boyer, "Dynamic modeling of a 3-D serial eel-like robot*," Proc. IEEE Int. Conf. Robot. Autom*., Barcelona, Spain, 2005, pp. 1282-1287.

[46] M. El Rafei, M. Alamir, N. Marchand, M. Porez and F. Boyer," Motion control of a three-dimensional eel-like robot without pectoral fins," *Proc of the 17th IFAC World Congress,* 2008, vol. 17, part 1.

[47] D. Trivedi, A. Lofti and C.D.. Rahn,"Geometrically exact dynamic models for soft robotic manipulators," *IEEE Int. Conf. Intel. Robot. Sys*., San Diego, CA, 2007, pp. 1497-1502.

[48] N. Li, T. Zhao and Y. Zhao, "The dynamic modeling of snake-like robot by using nominal mechanism method*," Intel. Robot. and Appl., Springer–Verlag*, Berlin–Heidelberg 2008.

[49] H. H. Mochiyama and T. Suzuki, "Kinematics and dynamics of a cable-like hyper-flexible manipulator," *Proc. IEEE Int. Conf. Robot. Autom*., Taipei, Taiwan, 2003, pp. 3672-3677.

[50] E. Tatlicioglu, I.D. Walker and D.M. Dawson, "Dynamic modeling for planar extensible continuum robot manipulators," *Int. Jour. Robot. Autom*., Vol. 24, No. 4, 2009.

[51] E. Tatlicioglu, I.D. Walker and D.M. Dawson, "New dynamic models for planar extensible continuum robot manipulators," *IEEE Int. Conf. Intel. Robot. Sys*., San Diego, CA, 2007, pp. 1485-1490.

[52] Y. Yekutieli, R. Sagiv-Zohar, R. Aharonov, Y. Engel, B. Hochner and T. Flash, "Dynamic model of the octopus arm I. biomechanics of the octopus arm reaching movement," *Journ. Neurophy*., vol. 94, 2005, pp. 1443-1458.

[53] E. S. Mallet, G. T. Yamaguchi, J. M. Birch, and K. C. Nishikawa, "Feeding motor patterns in anurans: insights from biomechanical modeling," *Journal of life sciences*, vol. 41, issue 6, pp. 1364-1374.

[54] N. Giri, I. D. Walker, "Continuum robots and underactuated grasping," *Mechanical Sciences,* vol. 2,pp. 51-58.

[55] http://web.mst.edu/~stutts/supplementalnotes/lagrangeeqn05.pdf

[56] H. Asada, "A geometric representation of manipulator dynamics and its application to arm design," *ASME Journal of Dynamic Systems, Measurement and Control*, vol. 105, pp. 131-142, 1983.

[57] T. Yoshikawa, "Manipulability of robotic mechanisms," *The International Journal of Robotics Research*, 1985, vol. 4, no. 2 3-9.

[58] T. Yoshikawa, "Dynamic manipulability of robot manipulators," *Proc. 1985 IEEE Conf. Robotics Automation*, 1985, pp. 1033-1038.

[59] I. D. Walker, "Impact configurations and measures for kinematically redundant and multiple armed robot systems," *IEEE Trans. on Robotics and Automation*, 1994, vol. 10, pp. 670-683.

[60] P. Chiacchio, "A new dynamic manipulability ellipsoid for redundant manipulators," *Robotica*, 2000, vol. 18, issue 04.

[61] P. Chiacchio, “Global task space manipulability ellipsoids for multiple-arm systems,” *Proc. of IEEE Conf. Robotics Automation*, 1991,vol. 7, pp. 678-685.

[62] I. A. Gravagne, I. D. Walker, “Manipulability, force and compliance analysis for planar continuum manipulators,” *IEEE Trans. on Robotics and Automation*, vol. 18, no.3.

[63] D. G. Cadwell, G. A. Merdrano-Cerda, and M. J. Goodwin, “Control of Pneumatic Muscle Actuators,” *IEEE Control Systems Journal*, vol. 15, no. 1, pp. 40-48, Feb 1995.

[64] L. Meirovitch, Methods of Analytical Dynamics, McGraw-Hill Book Company, 1970, pp. 46-100.

[65] N. Giri, and I. D. Walker, “Continuum robots and underactuated grasping,” *Proc. of IFToMM/ASME International Workshop on Underactuated Grasping (UG2010)*, August 2010, Montreal, Canada.

[66] N. Giri, and I. D. Walker, “Three module lumped element model of a continuum arm section,” *Proc. IEEE/RSJ International Conference on Intelligent Robots and Systems (IROS*), September 2011 (To be published).